# MODEL AND OBSERVATION COMPARISONS OF IONOSPHERIC CURRENT SYSTEMS

by

TRE'SHUNDA JAMES

Presented to the Faculty of the Department of Physics of

The University of Texas at Arlington in Partial Fulfillment

of the Requirements

for the Degree of

DOCTOR OF PHILOSOPHY

THE UNIVERSITY OF TEXAS AT ARLINGTON

May 2023

# DECLARATION OF AUTHORSHIP

---

I, **Tre'Shunda James**, declare that this dissertation titled, "Model and Observation Comparisons of Ionospheric Current Systems" and the work presented in it are my own. I confirm that:

• This work was done wholly or mainly while in candidature for a research degree at this University.

• Where any part of this thesis has previously been submitted for a degree or any other qualification at this University or any other institution, this has been clearly stated.

• Where I have consulted the published work of others,this is always clearly attributed.

• Where I have quoted from the work of others, the source is always given. With the exception of such quotations, this thesis is entirely my own work.

• I have acknowledged all main sources of help.

• Where the thesis is based on work done by myself jointly with others, I have made clear exactly what was done by others and what I have contributed myself.

Signed:

_____

Date:

_____

# ACKNOWLEDGEMENTS

I thank my advisor, my "academic father", Dr. Ramon E. Lopez for his guidance and pure intentions. Before I even knew he would be my advisor, he expressed genuine interest in my academic success.

I thank Dr. Alex Glocer for his insight on MHD modeling and help with proposals.

I thank my parents, Angela and Robert James for their unwavering support. They might not have always understood exactly what I was studying or why, but that never changed how much love and support they showed along the way.

I thank my sister LM, for enthusiastically allowing me to be her private tutor as she works her way through numerous programs and certifications.

I thank my emotional support animal, Tory, for being the best oversized lapdog and for occasionally dragging me away from my studies to accommodate his bed time.

I would also like to thank my friend JP for his encouragement, motivation, and accountability during my last semester. It's still that black abundance.

Additionally, I want to thank my partner HG, for challenging me, as if graduate school was not challenging enough. I also thank him for his love and support .

Lastly, I thank the committee for their time and feedback on this dissertation.

April 19, 2023

ABSTRACT

# MODEL AND OBSERVATION COMPARISONS OF IONOSPHERIC CURRENT SYSTEMS

Tre'Shunda James, Ph.D.

The University of Texas at Arlington, 2023

Supervising Professor: Dr. Ramon E. Lopez

The interaction between the dynamically changing solar wind and Earth's magnetosphere results in several different current systems. The most relevant to space weather are the Birkeland currents, a.k.a field-aligned currents (FACs), that couple the magnetosphere to the ionosphere. These currents flow into and out of the ionosphere and are closed through the ionosphere by the horizontally flowing eastward and westward electrojets. This FAC-electrojet current system is responsible for some of the most beautiful and detrimental space weather impacts. The aurora borealis (or northern lights) in the Northern Hemisphere and aurora australis (or southern lights) in the Southern Hemisphere are displays of lights resulting from energetic particles that have travels from the sun, through interplanetary space, down Earth's magnetic field lines and into Earth's polar region. These downward flowing particles are responsible for upward flowing FACs.

On the contrary, the FAC-electrojet current system can cause major disturbances. These ionospheric currents have been known to destroy satellites, erode

pipelines, and disrupt the power grid. The Space Weather Prediction Center (SWPC) use global magnetohydrodynamic (MHD) models to nowcast and forecast space weather in an attempt to forewarn society about potential space weather impacts.

So, it is imperative that we investigate the dynamics and processes that affect the magnitude of these ionospheric currents. To do this, we take a two way approach in which we first look to investigate how these currents behave in reality. Then we look to determine how well do global MHD models reproduce the observed behaviors and magnitudes of these currents. Specifically, we investigate the role seasonal inter-hemispheric asymmetry in conductance play in controlling the amount of ionospheric current using observations and simulating complementary models.

From observations we find that in the summer the currents increase in magnitude with increasing solar wind electric field and F10.7. In the winter, the currents decrease with increasing F10.7, as a consequence of a decreased geoeffective length. We also validate current-closure as seen by the observed FAC-electrojet relationship. This linear relationship is also reproduced by SWMF, despite the model's underestimation of the magnitudes of the currents and inability to replicate reality at times. The model does not always reproduce the behavior of the currents with increasing F10.7, but it does reproduce the expected behavior in the potential. This points to the need for improved conductivity models within global MHD models.

# TABLE OF CONTENTS

LIST OF ILLUSTRATIONS

LIST OF TABLES

# CHAPTER 1

## INTRODUCTION

Space weather is the study of how the solar wind interacts with the near-Earth environment and affect technology and society. The solar wind consists of charged particles and the Sun's magnetic field and it propagates from the Sun towards Earth, eventually interacting with Earth's geomagnetic field. Since, the solar wind originates at the Sun, our understanding of space weather does also. At the surface of the Sun there are phenomena such as Coronal Mass Ejections (CMEs), solar flares, and High Speed Streams (HSS) that contribute to the solar wind. CMEs are large explosions of plasma and magnetic field from the Sun's corona into the heliosphere. Solar Flares are flashes of of light, taking place near sunspots, in the Sun's lower atmosphere. Contrary to CMEs, solar flares occur very quickly, are more localized, and associated effects such as x-rays and high energy electrons travel at the speed of light, reaching Earth in approximately 8 minutes. HSS correspond to higher speed solar wind resulting from coronal holes (i.e., open solar magnetic field lines). These Sun-originating phenomena contribute to the interplanetary magnetic field (IMF) by transporting solar magnetic field into interplanetary space. These phenomena cause variations in the solar wind that deviates from the background IMF and are footprints for resulting space weather impacts on Earth.

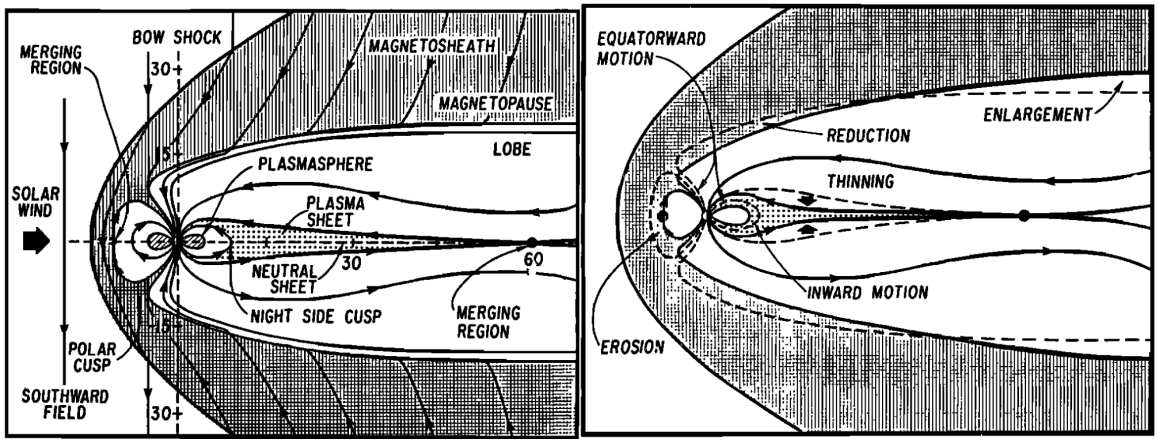


(a) Ground state configuration of the magnetosphere.

(b) Perturbed state of the magnetosphere after merging on the dayside.

Figure 1.1: From McPherron [1979] demonstrates the change in the magnetosphere, the shape of the magnetopause and position of the nose of the magnetopause.

## 1.1 Solar Wind-Magnetosphere (SW-M) Interaction

As the solar wind enters the geospace environment, it is abruptly slowed down at the bow shock which is the barrier between the solar wind and Earth's magnetosphere. The 'frozen-in' magnetic field or interplanetary magnetic field (IMF) travels beyond the bow shock and interact with Earth's magnetic field. The place where this interaction occurs on the dayside is considered to be the magnetopause. The exact location and shape of the nose of the magnetopause, which lies on the Earth-Sun line, varies as it depends on the balance of solar wind pressure, and the strength of the currents that shape the magnetosphere. Sibeck et al. [1991] conducted a statistical study of magnetopause crossings in which quantified the relationship between IMF $B_z$, region 1 Birkeland currents, the position of the nose of the magnetopause, and the shape of the dayside magnetosphere. The magnetopause is dynamic and is constantly changing in order to achieve pressure balance with the varying solar wind. Figure 1.1b shows the change in position of the magnetopause when perturbed.

### 1.1.1 Magnetic Reconnection

Along the magnetopause, magnetic reconnection occurs. Magnetic reconnection is a process that results from the merging of magnetic field lines. When plasma carrying magnetic fields become close to one another, these field lines are broken and rejoined into a new configuration and this change in configuration releases stored energy. In the geospace environment, magnetic reconnection occurs between the IMF and Earth's magnetic field. As the solar wind merges with the geomagnetic field, magnetic reconnection occurs at places of favorable field line orientation – the most favorable being southward IMF ($-B_z$). When southward IMF enters the near-Earth environment, magnetic reconnection occurs on the day-side and momentum, kinetic energy, and particles are transferred along the newly configured field lines into the magnetotail. Once enough energy has built up in the magnetotail, opposing field lines, once again, allows for magnetic reconnection on the night, as shown in Figure 1.1.

As a result of magnetic reconnection in the tail, energy and particles are transported along field lines and into Earth's auroral region; this process is known as a substorm [McPherron, 1979]. Substorms have three phases: the growth phase, the expansion phase, and the recovery phase. The growth phase is characterized by the the change in orientation of $B_z$. The accompanying motion of the plasma causes an electric field which is projected along field lines into the ionosphere and since the ionosphere acts as an conductor, electric currents are allowed to flow into and throughout the ionosphere. These currents are known as Birkeland currents, Pedersen currents, and Hall currents. A more detailed description of these currents and their configuration is provided later in this chapter.

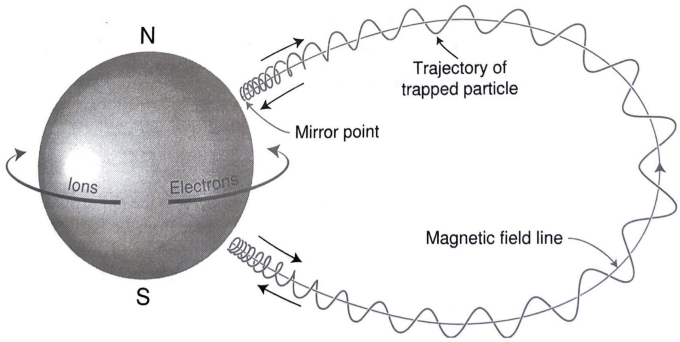


Figure 1.2: Figure 3.1 from Baumjohann and Treumann [2012] illustrates the bounce, gyration, and mirror motions of trapped particles in Earth's magnetic field.

When $B_z$ turns southward, this transport of plasma and magnetic flux from the dayside to the tail and back to the dayside; this process is known as magnetospheric convection marks the commencement of a growth phase of the substorm [McPherron, 1970, Erickson and Wolf, 1980]. The growth phase is associated with the enhancement of magnetospheric convection that in turn enhances the electric field. The growth phase continues as magnetospheric flux from the day side is built up in the tail. Where, once enough flux has built up in the tail, magnetic reconnection occurs and field lines collapse inward transporting particles into the ionosphere. These precipitating particles increase the ionospheric conductivity. Additionally, this increase in precipitating particle result in the expansion of the auroral oval poleward (i.e., auroral bulge). Once, this auroral bulge begin to move equatorward, the substorm is now in its recovery phase. In this phase, the intensity of the currents also decreases and the system progressively relaxes back to its undisturbed state.

Trapped particles gyrate, bounce, and undergo a slow azimuthal drift in Earth's magnetic field (Figure 1.2) The Earth's magnetic field can be approximated as a dipole, where the field strength is minimal at the equator and becomes maximum, along the same field line, at Earth's polar region. Along these field lines, trapped

particles bounce back and forth between their northern and southern hemisphere mirror points. Some of these particles, with a large enough pitch angle, are able to escape this bounce motion and precipitate into the ionosphere. The trapped particles exhibit single particle motion that consequently require them to gyrate around the field line, with increasing frequency of gyration in stronger magnetic fields. Due to the gradient and curvature of these field lines, the particles also drift around Earth in the azimuthal direction. The ions drift westward and the electrons drift eastward. The associated current with these particle drifts is known as the ring current.

The total current generated by these drifting ring current particle creates a magnetic disturbance that can be detected by ground based magnetometers in and near the equatorial region. The magnitude of this disturbance is relatively small during quiet times. During what is considered to be storm time, geomagnetic storms originating in the tail inject a large number of particles into the ring current. This large increase in the ring current creates a larger depression in Earth's equatorial magnetic field. The change in the magnetic field as a consequence of increased ring current is often quantified by the Disturbance storm time (Dst) index. This index, is derived from 4 ground magnetometers in the equatorial region (see Sugiura and Kamei [1991] for a full description and derivation of Dst index)

Contrary to substorms, geomagnetic storms occur when periods favorable to dayside merging and magnetic reconnection persist for extended periods of time. Substorms can occur on a timescale of hours, while geomagnetic storms can take place over a period of days. Another difference between substorms and storms is significant ring current development.

On the dayside, as previously mentioned, magnetic reconnection produces an electric field as flux merges and crosses the merging line this electric field has magnitude $VB_z$. Using Faraday's law and integrating this EMF, you can determine the

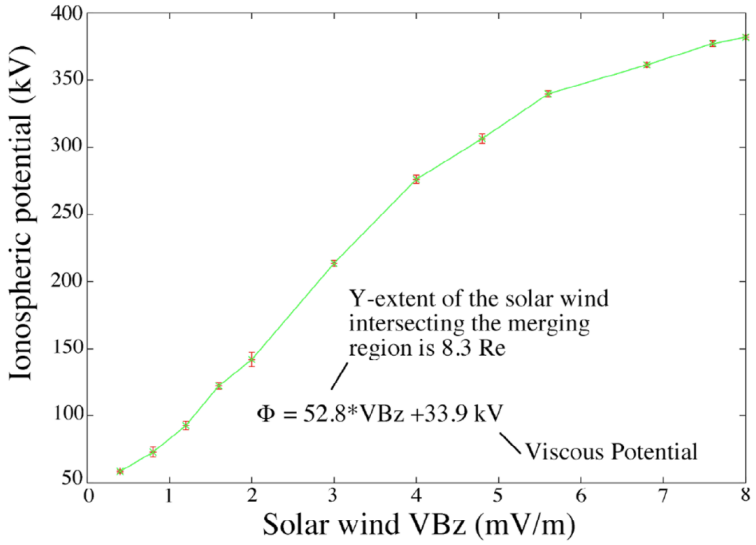


Figure 1.3: From Lopez et al. [2010] displays the relationship between the ionospheric potential and solar wind electric field. Up to about 3mV/m the relationship is linear. Thereafter, the potential saturates.

associated potential drop across the ionosphere from dawn to dusk. The relationship between negative $B_z$ and this potential drop is split into two regimes. For small values of negative $B_z$, this potential drop is linear but for larger values of negative $B_z$, the potential saturates. Lopez et al. [2010] shows the saturation of ionospheric potential using a global magnetohydrodynamic (MHD) model (Figure 1.3). More details about such MHD codes will be presented in Chapter 3.

These authors also show such saturation effect by determining the ionospheric potential from solar wind streamline analysis. Solar wind streamlines tracks the flow of the solar wind that reaches the merging region. The y-extent of the flow lines that reach the merging region, also known as the geoeffective length, is multiplied by the solar wind electric field to determine the potential due to reconnection for each run.

Moreover, the authors attribute the behavior of the reconnection potential as a response to increasing southward IMF to the magentosheath force balance. The momentum equation is given as:

$$\rho \frac{d\vec{V}}{dt} = -\nabla P + \vec{J} \cdot \vec{B}, \tag{1.1}$$

for a time-independent solar wind around a magnetosphere that has come to equilibrium with the flow. The LHS of the equation, in this case, represents the divergence of the solar wind flow around the magnetosphere and the RHS of the equation represent the pressure gradient and magnetic forces in the magnetosheath, respectively. In this scenario, the LHS of the equation is balanced my the magentosheath forces. The authors argue that during periods of small IMF, the first term on the RHS dominates the flow and that when IMF increases past a certain value there is a regime shift to where the magnetic force dominates and the ionospheric potential saturates. This shift occurs because for large IMF, the divergence of the flow increases and the amount of solar wind flow that reaches the merging line decreases.

Reconnection also occurs at high latitudes during northward IMF, however, in this dissertation we focus on southward IMF because it is the most important for space weather impact.

### 1.1.2 The Viscous Interaction

There is also a second, less efficient (Tsurutani and Gonzalez [1997]), mechanism for the transport of momentum across the magnetopause, known as the viscous interaction [Axford and Hines, 1961]. As the solar wind blows past the magnetosphere it will carry magnetospheric plasma from the most outer region of the magnetosphere anti-sunward down the tail. As this plasma builds up in the tail, it exhibit a return flow sunward from further inside the magnetosphere, forming the convection pattern or viscous cells as seen in Figure 1.5. This convection is then transported along field lines and mirrored into the ionosphere. The viscous interaction also have an accompanying potential and electric field. Close examination of Figure 1.3, reveals

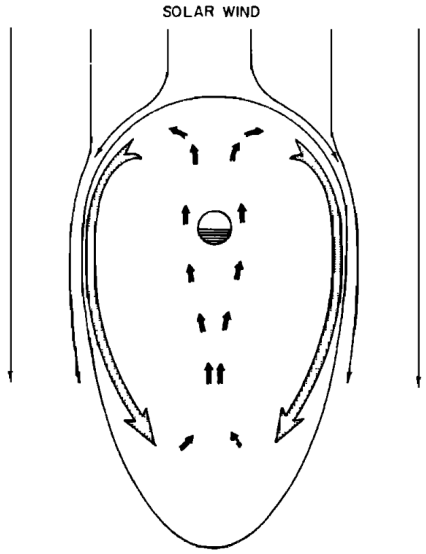


Figure 1.4: Figure 3 from Axford and Hines [1961] shows the convection pattern in the magnetosheath as a consequence of the viscous interaction.

the viscous potential is a constant that serves as justification of why the potential does not go to zero as IMF $B_z$ becomes zero. The viscous interaction exists for all orientation of IMF. The previously mentioned potential resulting from the merging region is about ten times the potential from this viscous interaction (Reiff and Luhmann [1986], Boyle et al. [1997], Hairston et al. [2003]). The overall ionospheric (or cross polar cap) potential is a sum on the viscous potential and magnetic reconnection potential, for southward IMF (Lopez et al. [2010], Bruntz et al. [2012] ). The velocity sheer created by the viscous cells generate Birkeland currents of the same polarity as Region 1 Birkeland currents.

## 1.2 Magnetosphere-Ionosphere (M-I) Coupling

Birkeland currents consist of two current systems that can be differentiated by the latitude and the direction in which they flow into Earth's polar region [Iijima and

Potemra, 1976]. The Region 1 (R1) Birkeland current flows into the ionosphere on the dawn side and out of the ionosphere on the dusk side. This current transmits solar wind stress to the ionosphere and its magnitude depends on the amount of solar wind-magnetosphere coupling [Lopez et al., 2010]. The Region 2 (R2) Birkeland current is driven by plasma pressure gradients in the inner magnetosphere. This current flows in the opposite polarity to Region 1 and is found at a lower latitude than the former (e.g, Ganushkina et al. [2018]). These currents are closed by the horizontally flowing currents in the ionosphere. There are two types of currents that flow horizontally in the ionosphere: Hall and Pedersen Currents. The Pedersen currents flow in the direction of the electric field and over the polar cap while the Hall currents forms a two-cell convection pattern that flow perpendicular to electric field and magnetic field. The components of the Hall currents that flow between the R1 and R2 Birkeland currents are known as the eastward and westward auroral electrojets. All of these currents cause magnetic perturbations in the Earth's magnetic field. The configuration of the currents described here is shown in Figure 1.6.

Since the FACs couple the magnetosphere to the ionosphere, the magnitude of these currents can be measured using in-situ magnetometers. There are a number of missions and satellites equipped with these magnetometers that collect Birkeland current data. The Active Magnetosphere and Planetary Electrodynamics Response Experiment (AMPERE) derives data products from engineering magnetometers on-board the Iridium satellite constellation. These 66 Iridium satellites are situated in polar orbits at about 780km above Earth in six equally spaced planes. Each magnetometer measures the satellite's cross-track magnetic field and from this measurement the data is processed using a spherical harmonic fitting technique to obtain the FACs (Anderson et al. [2000b], Waters et al. [2001b]). The latest AMPERE data products are available online (https://ampere.jhuapl.edu). The total Birkeland current data is

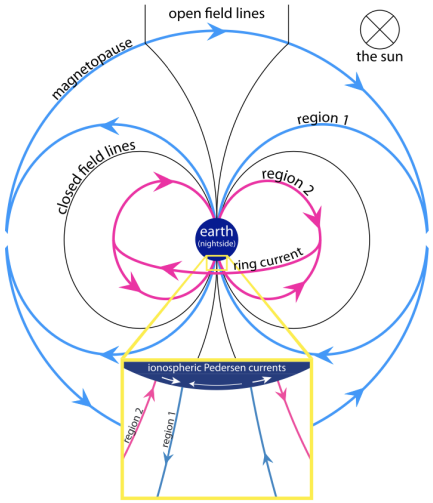


(a) From Coxon et al. [2014] shows the electrical current systems from the night side. In blue, the R1 currents and magnetopause are shown. The pink shows the R2 and ring currents. Outlined in the yellow box, the ionospheric Pedersen currents are shown flowing across the R1, R2, and polar cap.

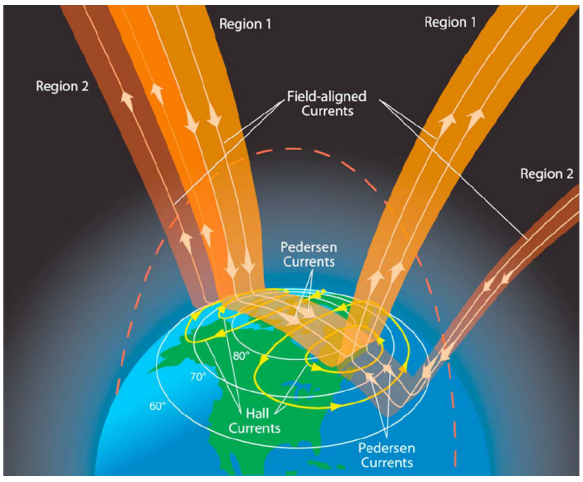


(b) From Le et al. [2010] displays the configuration of the ionospheric currents and the FACs.

Figure 1.5: The configuration of currents that couple the magnetosphere to the ionosphere.

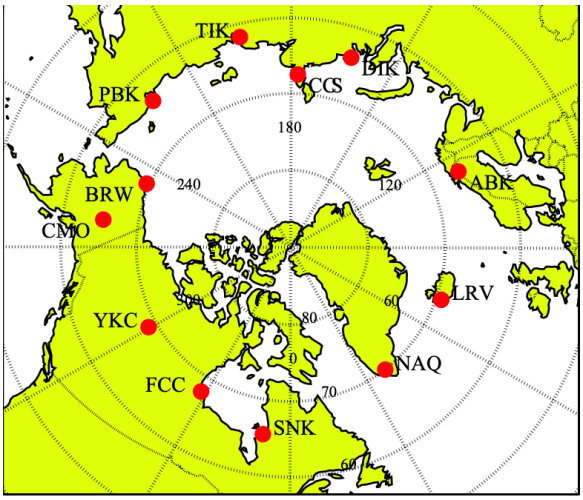


Figure 1.6: From Tomita et al. [2011] shows the location of the 12 magnetometer stations used to derive AE index. These stations lie within 60 degrees geomagnetic latitude.

provided with a two minute cadence. Global maps of the Birkeland current can be generated online in both northern and southern hemispheres for 10 minute intervals.

To measure the currents flowing horizontally in the ionosphere, ground based magnetometers are used. Because these magnetometers are at fixed station locations, spatial resolution has been an ongoing feat in accurately measuring these currents. Eastward flowing currents produces a southward perturbation in the magnetic field and westward flowing currents produces a northward field perturbation. The eastward and westward electrojets are often characterized using the Auroral Electrojet (AE) index. The 12 AE observatories are located in the auroral region in the northern hemisphere. The location of these observatories are shown in Figure 1.6. The AE data is first normalized by averaging the five international quiet days for each station for a month and subtracting that average value from each one- minute value measured at that station for that month. At a given time, the largest and smallest values are selected from each station. The largest magnetic perturbation is considered the AU, which is the largest eastward electrojet. The smallest value is considered the AL

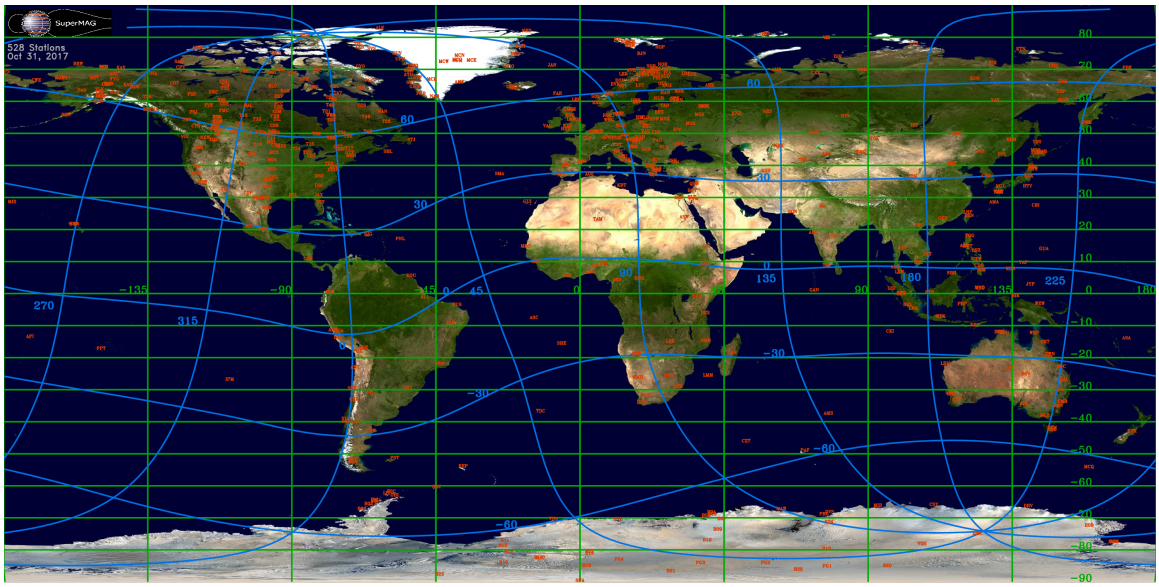


Figure 1.7: From SuperMAG website (`https://supermag.jhuapl.edu/`). The location of the ground magnetometer stations used to derive SME.

and this is the largest westward electrojet. AE and AL form an envelope, where the difference between AL and AU is the AE index. The average of AL and AU is the AO index. The AO index provides a measure of the equivalent zonal current.

Another index used to quantify the overall activity of the electrojets is the SuperMAG Electrojet (SME) index. This index is derived in the same manner as AE, but from a larger number of ground magnetometer stations. SuperMAG consists of more than 300 ground based magnetometers, as shown in Figure 2.1. Each of these stations are operated by independent contractors who provide there geomagnetic data to the SuperMAG team to be processed. The derived data products include, but are not limited to, the following auroral electrojet indices: SME, SML, and SMU which are analogous to AE, AL, and AU, respectively. The SuperMag data is available at `https://supermag.jhuapl.edu/` in one minute increments. SuperMAG also allows for the customization of the data products through the section of stations.

## 1.3 Magnetosphere-Ionosphere-Thermosphere (M-I-T) Coupling

The M-I-T coupling is quite intricate. The FAC that couple the M-I are closed in the ionosphere by the electrojets and this ionospheric current system affects ionospheric conductivity. The changes in M-I coupling often lead to changes in IT variables such as density, temperature, total electron content, neutral and ion winds and composition, electric fields, currents, and conductivities.

Originating in the magnetosphere and trapped in closed magnetic loops, particles bounce and drift along closed field lines. At small enough pitch angles, these particles can escape the magnetosphere and precipitate into the ionosphere. When these electrons collide with neutral atmosphere ions, radiation is produced in the visible wavelengths. These visible displays of light in the upper atmosphere are known as the aurora. There are several different types of ion and electron precipitation. Newell et al. [2009] defines diffuse, broadband, and monoenergetic precipitation and their role in the global particle precipitation budget. There are also other mechanisms, besides reconnection, that accelerate particles into Earth's ionosphere. These mechanisms are not well understood, but the effect that precipitating particles have on the conductivity of the ionosphere is. As these particle collided with neutral atoms in the ionosphere, these atoms are then ionized and the ionospheric conductivity is increased.

Aside from particle precipitation and ionospheric currents, ionospheric conductivity is also affected by solar EUV flux. Solar EUV radiation originating in the Sun atmosphere travel towards Earth and is absorbed into Earth's upper atmosphere. These photons ionize the upper atmosphere, contributing to its conductivity. Since the EUV radiation never reached the ground and it is difficult to take direct measurements, the amount of EUV flux is usually quantified using F10.7 cm radio flux (

F10.7 index) as a proxy. The F10.7 index is a measurement of total emission from the solar disk at a wavelength of 10.7 cm. Each measurement is made over a 1 hour period centered on the epoch of time. The value is measured in solar flux units (sfu) and though it is often referred to as F10.7 flux, it is actually a flux density. A more detailed description of measurement acquisition and calculations is provided by Tapping [2013].

These changes in conductivity also effect the amount of current. Using Ohm's law, the relationship between the Hall, Pedersen, and Birkeland currents can be expressed as:

$$\vec{j} = \Sigma_P \vec{E_\perp} + \Sigma_\parallel \vec{E_\parallel} - \Sigma_H \frac{(\vec{E} \times \vec{B})}{B}, \tag{1.2}$$

where $\vec{E}$ is the electric field, $\vec{B}$ is the magnetic field, and $\sigma$ is the conductivity. By taking the divergence of the horizontal component of this equation, assuming current continuity, the Birkeland current is:

$$\vec{j_\parallel} = \Sigma_P \nabla \cdot \vec{E} + \vec{E} \cdot \nabla \Sigma_P + \frac{(\vec{E} \times \nabla \Sigma_H) \cdot \vec{B}}{B}. \tag{1.3}$$

From this equation, it is clear that the Birkeland current dependence on the Hall and Pedersen conductances.

## 1.4 Interhemispheric Asymmetries

Though the Earth's magnetic field can be approximated by a symmetric dipole, it is not. The interhemispheric asymmetry in Earth's geomagnetic field strength and pole offsets lead to differences in plasma convection, neutral winds, total electron content, ion outflow, ionospheric currents and auroral precipitation [Laundal et al., 2017]. Here I focus on asymmetries in plasma convection, ionospheric currents and auroral precipitation, as they relate to the research done in this dissertation.

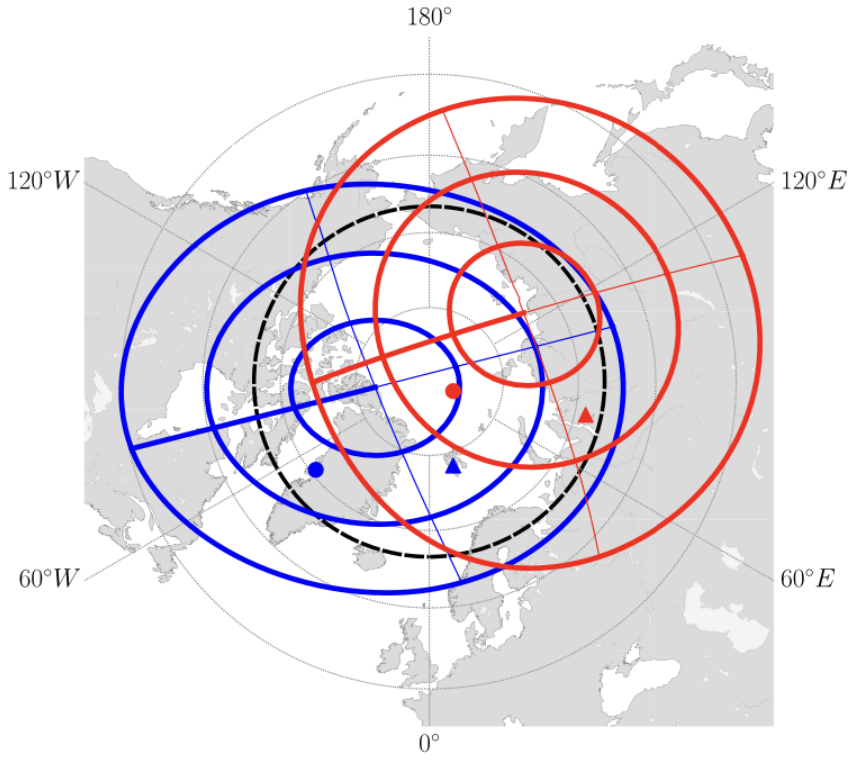


Figure 1.8: From Laundal et al. [2017]. The Magnetic QD grids from both hemispheres (red is South, blue is North) shown in geographic coordinates, projected to the NH. Conjugate stations are represented by circles and triangles. The offset between the magnetic and geographic poles is shown

The offset between the Northern and Southern poles in geographical and magnetic coordinates means that during certain times one hemisphere will receive more sunlight than the other and thus will be more conducting than the other. This change in conductivity has been found to be a consequence of the change in ionospheric and magnetospheric convection (e.g., Ruohoniemi and Greenwald [2005], Pettigrew et al. [2010], Ridley et al. [2004]), which is dependent on the north-south asymmetry in the magnetic field.

The polar caps lie within the auroral regions and they are regions threaded by equal amounts of open magnetic flux in the two hemispheres. The electric field generated from magnetic reconnection flow across this polar cap and the maximum

difference in the electric potential is known as the cross polar cap potential (CPCP). Asymmetries in the magnitude of the CPCP have been both observed and quantified. Studies have shown the CPCP to be slightly stronger in the Southern hemisphere as compared to the Northern hemisphere (Förster and Cnossen [2013], Pettigrew et al. [2010], Papitashvili and Rich [2002], Förster and Haaland [2015] ).

Because of the change in ionospheric conductivity, currents that flow into and within the ionosphere also exhibit interhemispheric asymmetrical behavior (c.f., Equations 1.2 and 1.3 ). The Birkeland current depends on the Hall and Pedersen conductances. As these conductances experiences interhemispheric asymmetry, so do the Birkeland current and associated Hall and Pedersen currents.

## 1.5 Space Weather Impacts

These currents flowing in the ionosphere play an important role in the space weather effects society might encounter. For example, the process in which the thermosphere expands because of frictional heating caused by these electrical currents dissipating energy into the ionosphere, known as Joule Heating (e.g., Brekke and Kamide [1996], McHarg et al. [2005]), causes the atmosphere to expand and increase satellite drag, which can lead to the loss of satellites in low earth orbit [Wilson et al., 2006, Chen et al., 2012]. This is exactly what happened on 4 February 2022 when nearly 40 Space X Starlink satellites were destroyed. Dang et al. [2022] describes the events that created the geomagnetic disturbances, originating at the Sun all the way to the low Earth orbiting (LEO) atmosphere. On 3 February 2022, the Falcon 9 rocket launched 49 Starlink satellites into LEO. During an shortly after the launch, there were two CMEs as a result of solar flares that reached Earth. As a results, a geomagnetic storms occurred, the ionosphere became more conducting, the magnitude

of the ionospheric current increased, and additional Joule heating lead to an increase in atmospheric drag. These Starlink satellites were intended to provided internet to remote locations. The societal impact of the loss of these satellites are clear– remote locations will not be able to receive internet as a result of the constellation. However, the economical impacts related to the loss of these satellites are arguably even more substantial. It is estimated that the financial loss of these satellites totalled several tens of millions of dollars [Hapgood et al., 2022].

Other adverse affects include ground induced currents (GICs) which result from large-amplitude, rapidly changing geomagnetic disturbances in Earth's magnetic field. These periods are directly related to enhanced ionospheric currents and enhanced FACs that often traces back to CMEs. The most historical event resulting from a CME is the Carrington Event. On 1 September 1859, Carrington [1859] and Hodgson [1859] both identified two bright flares while observing the Sun. In less than 18 hours later, there was a geomagnetic storm on Earth. This storm was the largest every recorded geomagnetic storm. In the wake of the storm telegraph networks experiences disruptions and outages caused by GICs associated with the geomagnetic storms. During large geomagnetic storms the aurora oval moves equatorward (Yokoyama et al. [1998], Blake et al. [2021]). During the Carrington Event, these aurora were seen as far equatorward as Hawaii. These aurora were so intense that telegraph workers were able to use these currents to transmit and receive telegraphic dispatches [Prescott, 2022].

Beyond, power networks [Pulkkinen et al., 2017] and satellites, space weather phenomena can also affect pipelines [Pirjola et al., 2000], and railways [Eroshenko et al., 2010]. Thus, the understanding of the dynamics of the ionospheric current systems and how their behavior changes is essential in mediating space weather impacts.

Through observations and model validation, I investigate the solar EUV driven interhemispheric asymmetry in these ionospheric currents. In Chapter 2, I investigate how Birkeland currents and electrojets behave during the winter and summer solstice periods using observations. Chapter 3 I describe magnetohydrodynamic (MHD) models and their applications to space weather. In Chapter 4, I investigate the ability of global magnetohydrodynamic models to replicated the observed current system behavior and magnitudes. In Chapter 5, I provide concluding remarks and future work.

# CHAPTER 2

## ASYMMETRIES IN IONOSPHERIC CURRENTS

## The Effect of F10.7 on Interhemispheric Differences in Ionospheric Current During Solstices

**Coauthor:** Ramon E. Lopez

### Citation

James, T., Lopez, R. E. (2022). The effect of F10.7 on interhemispheric differences in ionospheric current during solstices. Advances in Space Research, 69(8), 2951-2956.

## SUPPLEMENT

This observational study published in Advance in Space Research highlights the behavior of the ionospheric electrojets and Birkeland currents in response to change in conductivity between solstices. Theoretically, since the current in the ionosphere must be divergence free, the Birkeland currents must then be closed in the ionosphere. This work is the first to quantify the relationship between the electrojets and Birkeland currents (Figure 2.3). We determined the Birkeland current flowing into the ionosphere is approximately 107 times the auroral electrojets. Additionally, this study determined this relationship to be consistent across seasons which implies the configuration of the current closure to be independent of ionospheric conductivity.

ABSTRACT

We investigate the differences in the electrojet and Birkeland current systems during summer and winter solstice and the effect of F10.7. The difference in solar illumination of the polar ionosphere during the winter versus summer solstice results in significantly higher conductivity in the summer polar ionosphere. As expected, the currents are larger during the summer than during the winter. The relationship between the electrojets and the Birkeland current systems is essentially constant across seasons, as expected if the ionospheric electrojets close the Birkeland currents. The magnitude of F10.7 is an indicator of the level of solar-generated ionospheric conductance, therefore, one would expect larger ionospheric currents during periods of larger F10.7. This holds true for the summer solstice periods, however, the opposite trend is observed during the winter solstice periods. We provide an explanation for this finding based on the control of the dayside merging rate by the magnetosheath flow pattern.

## 2.1 Introduction

Large-scale field-aligned currents couple the magnetosphere to the ionosphere. These currents, known as Birkeland currents, consist of two current systems that can be differentiated by latitude and the direction in which they flow into Earth's polar region depending on the local time [Iijima and Potemra, 1976]. The Region 1 Birkeland currents flow into the ionosphere at dawn and out of the ionosphere at dusk at high latitudes near the open-closed field line boundary. This current transmits solar wind stress to the ionosphere, and its magnitude depends on the amount of solar wind-magnetosphere coupling [Lopez et al., 2010, Lopez, 2016], which is primarily the result of merging between the IMF and the geomagnetic field. There is an additional energy transfer mechanism, the viscous interaction [Bruntz et al.,

2012] that also drives Region 1 currents (at somewhat lower latitudes). However, the primary mechanism for the transfer of the energy and momentum from the solar wind to the magnetosphere-ionosphere system is driven by the merging interaction [Newell et al., 2008]. The merging interaction under most conditions can be considered to be proportional to the solar wind electric field, but under conditions of low solar wind Mach number, the dayside merging rate saturates [Borovsky and Birn, 2014, Lavraud and Borovsky, 2008, Lopez et al., 2010, Lopez, 2016]. Under these conditions the correlations between ionospheric currents and the typical solar wind coupling functions are weaker [McPherron et al., 2015].

The Region 2 Birkeland currents are driven by plasma pressure gradients in the inner magnetosphere, they flow in the opposite polarity to Region 1, and are found at lower latitudes than the former [e.g., Ganushkina et al., 2018]. The Birkeland currents close through the auroral electrojet, which is the horizontal current in the auroral region of the ionosphere. The magnitude of the electrojets are indexed by finding the largest northward or southward perturbation from ground magnetometers. The largest observed northward perturbation in nT, which is positive in the HDZ coordinate system, is an indicator of the largest eastward electrojet and is called AU. The largest observed southward perturbation in nT, which is negative in the HDZ coordinate system, is an indicator of the largest westward electrojet and is called AL. The AE index is defined as AU minus AL, and it is a measure of the global level of activity of the electrojets [Davis and Sugiura, 1966].

Given a certain ionospheric potential produced by the interaction of the solar wind with the geospace system, currents will flow with the magnitude of the current depending on the ionospheric conductivity. Ionospheric conductivity is driven in part by solar extreme ultraviolet (EUV) radiation [Ridley et al., 2004]. Solar ultraviolet radiation is dependent on solar zenith angle and the level of electromagnetic radiation

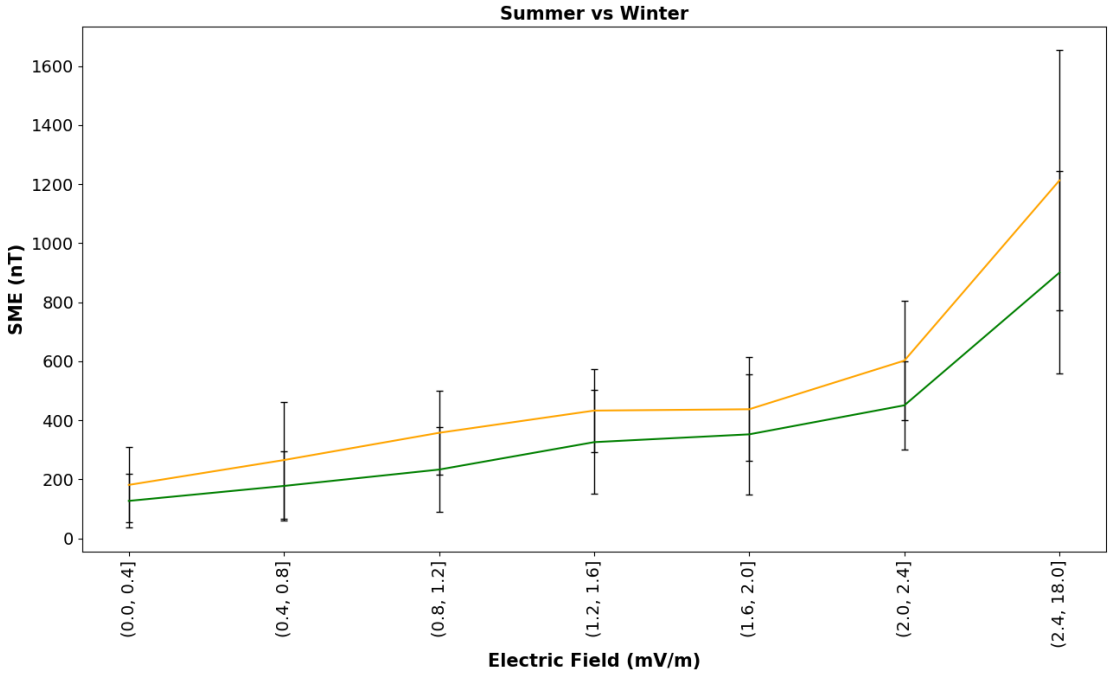


Figure 2.1: SME vs Solar Wind Electric Field. The weeks centered on the summer solstice are plotted in yellow. The green data are for the weeks centered on the winter solstice. The electric field is binned in 0.04 mV/m increments, except for the last bin in which the Mach number is low and the current has saturated.

produced by the Sun, which is typically quantified using the F10.7 index. Increased solar illumination increases ionospheric conductivity, in which, in return, increases the intensity of Region 1 currents [Fujii and Iijima, 1987]. The horizontal ionospheric currents also depend on the solar illumination. Ohtani et al. [2019] found that the magnitude of the dayside electrojets where controlled by the solar zenith angle, while the nightside electrojets also included a dependence on the dipole tilt angle. However, as seasons change the amount of EUV radiation seen by Earth's polar cap varies drastically. During the summer, the northern polar cap is entirely illuminated, but during the winter this same region receives almost no sunlight; and because EUV provides the baseline conductivity of the ionosphere, the currents flowing in the ionosphere exhibits a seasonal asymmetry.

Previous work has quantified this seasonal asymmetry in terms of the magnitude of the Birkeland currents [e.g., Juusola et al., 2009, Papitashvili et al., 2002, Ohtani et al., 2005]. Juusola et al. [2009] reported the Birkeland current in the summer to be 1.4 times larger than that in the winter, which is also well within the range of the 1.35 ratio reported by Papitashvili et al. [2002]. Similarly, Weimer et al. [1990] investigated the seasonal variation of AE and the relationship to the ionospheric potential. However, no work has yet quantified the seasonal asymmetry of electrojet magnitude using SME (SuperMag Electrojet, see Gjerloev [2012b]) which is a more global measure than the AE index. In this work we do just that. Moreover, we investigate the correlation between SME and the total Birkeland current, and the variation of these quantities with F10.7.

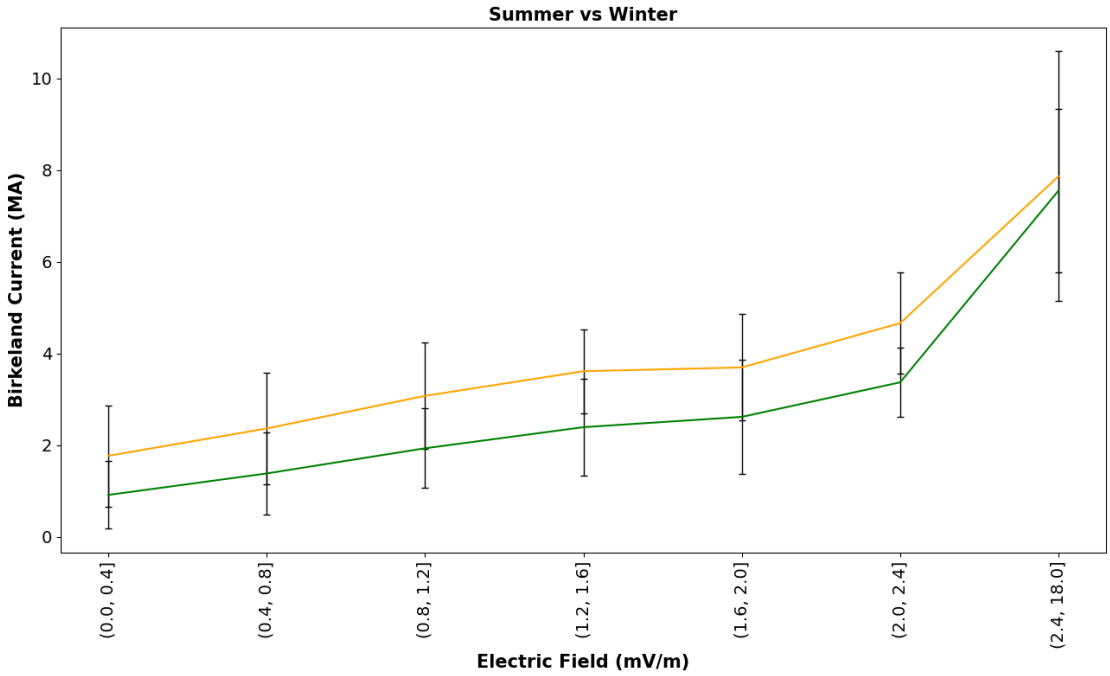


Figure 2.2: Birkeland Current vs Solar Wind Electric Field. The data are binned in 0.4 mV/m increments, except for the last bin. In yellow are the data for the summer weeks and the green are the data for the winter weeks.

## 2.2 Data and Observations

We conduct this study of the seasonal asymmetry in ionospheric current using SME as a measure of the strength of the auroral electrojets and the Birkeland currents in the northern hemisphere using data from AMPERE (`http://ampere.jhuapl.edu/products/itot/`). AMPERE collects data from the Iridium satellite system, which comprise over 70 satellites, each equipped with a magnetometer. The magnetic field data provides global maps of Birkeland currents [Anderson et al., 2000b]. The data used in this study span the years of 2010-2017, excluding the years associated with AMPERE data gaps, and are centered on the weeks of the summer and winter solstices to maximize the difference in solar illumination. The summer solstice weeks used were June 18-24 for years 2010-2013 and 2015-2017, while the winter solstice weeks used were December 18-24 2010-2013 and 2015-2016. Moreover, since we average over the entire week, the dipole tilt angle dependence of the nightside electrojets discussed by Ohtani et al. [2019] should average out, leaving just the solar EUV dependence. We use the SME index data from SuperMag (`http://supermag.jhuapl.edu/indices/`), which is derived from approximately 110 ground-based magnetometers stations. The SMU index represents the eastward electrojet (and corresponds to AU), while the SML index represents the westward electrojet (and corresponds to AL). SME is the difference between SMU and SML, just as AE is the difference between AU and AL. We use the SME index instead of AE, because it is derived from many more stations, allowing for a more accurate global measure.

To quantify the driver of the SME index, we use the solar wind electric field from the OMNI data set. We obtained the OMNI data from CDAWeb (`https://cdaweb.gsfc.nasa.gov/pub/data/omni/high_res_omni/monthly_1min/`). The data are taken the 1-week periods centered on the winter and summer solstices and

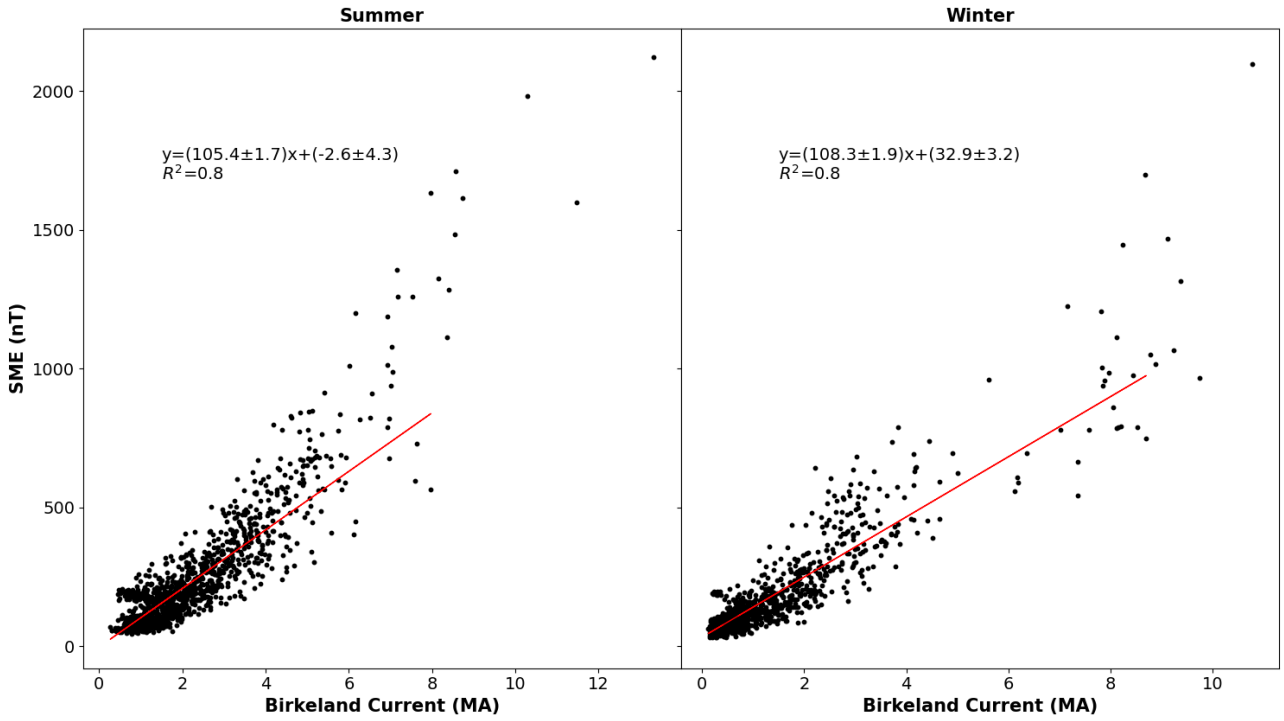


Figure 2.3: The relationship between SME and total Birkeland Current for weeks centered on the summer solstice (left) and weeks centered on the winter solstice (right).

are binned by solar wind electric field (0.4 mV/m intervals of southward IMF), except for the largest values of the solar wind electric field where there are a smaller number of points. Those were put into a single bin. The Birkeland current data from the AMPERE website and the solar wind data were averaged over 1 hour. The solar wind data have not been lagged relative to the SME and Birkeland current data. We did examine if shifting the solar wind data by 5 or 10 minutes relative to the other data sets made a difference, but we found essentially no change in the results to be presented here.

The integrated dayside reconnection rate, which is a measure of the energy transfer from the solar wind to the magnetosphere, is proportional to the solar wind electric field for magnetosonic Mach number $> 4$ [Lopez, 2016]. Therefore, we plot

SME vs Electric Field (Figure 2.1). Upon visual inspection, it is evident that the average value of the SME index in the summer is higher than that in the winter. On average, taking the summer-winter ratio in each bin, the average SME index in the summer is approximately 1.4 times greater than it is in the winter.

The Birkeland current exhibits the same behavior as the SME index as a function of solar wind electric field. The last bin is a cumulative bin including periods when the dayside merging rate is saturated [Lopez et al., 2010]. When saturation occurs, the dayside merging rate (and thus the ionospheric potential) becomes insensitive to the magnitude of the solar wind electric field and depends on other factors, such as solar wind density. We find that the summer-winter ratio of the Birkeland current magnitude under unsaturated conditions is about 1.6 (Figure 2.2).

We have also correlated the relationship between the SME index and the Birkeland current across season, presented in Figure 2.3. We only use data with SME values less that 750 nT to avoid extremely active periods when factors like saturation of the ionospheric potential could complicate the relationships [McPherron et al., 2015]or sudden extreme values of the SME index or the Birkeland currents could produce outlier points that unduly influence the linear fits. The slopes of the linear fits for the SME index as a function of the Birkeland current fall within each others error bars. This means that the relationship between the SME index and Birkeland Current is essentially independent of ionospheric conductivity, as it should if there is one big current system in which the eastward and westward electrojets close the Birkeland currents.

Additionally, we investigated the dependence of the magnitude of the currents on the value of the F10.7 index. Because the F10.7 index is a proxy for the solar EUV flux, we expect greater F10.7 to correlate with greater ionospheric conductivity and larger values of the currents for a given solar wind electric field. The summer and

Table 2.1: F10.7 Variance[a]

| Number of Hours (total, high, low) | Avg. SME [nT] (total, high, low) | Avg. Birkeland Current [MA] (total, high, low) | Avg. Solar Wind Electric Field [mV/m] | Avg. F10.7 (total, high, low) |
|---|---|---|---|---|
| 203 | 182.9 | 1.8 | | 96 |
| 67 | 214.3 | 2.0 | 0.2 | 127.0 |
| 67 | 136.4 | 1.5 | | 75.2 |
| 189 | 127.2 | 0.9 | | 107.8 |
| 63 | 108.4 | 0.8 | 0.2 | 137.4 |
| 63 | 147.1 | 1.1 | | 74.0 |

[a]The top three rows of data are for the summer and the bottom three rows of data are for the winter.

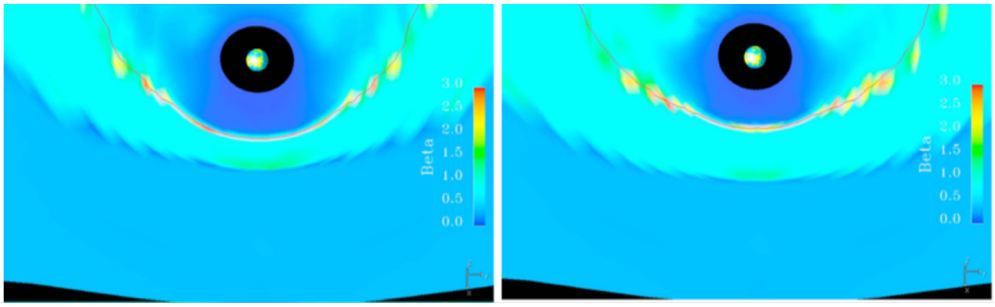


Figure 2.4: The panels are generated by a global magnetosphere simulation [Lopez et al., 2010]. This figure displays the position of the magnetopause (black line) with a conductivity of 5 mho (left) and 10 mho (right) for identical solar wind conditions with southward IMF.

winter solstice weeks data for the lowest electric field bin (0.0 mV/m-0.4 mV/m) were separated into 3 bins of F10.7: an overall average bin, a high bin (top third of F10.7 values), and a low bin (bottom third of F10.7 values). We find that, as expected, during the summer solstice weeks the value of the SME index and the total Birkeland current increased with F10.7. However, the opposite trend was observed during the winter solstice weeks; higher F10.7 is correlated with lower values of both the SME index and the total Birkeland current(Table 5.1). Other solar wind electric field bins (which have fewer points) exhibit the same trend. This is a surprising and seemingly counter-intuitive result.

## 2.3 Findings and Discussion

This work has demonstrated quantitatively that the average total Birkeland current and the average SME are larger in the summer than in the winter. These results are in agreement with previous studies. Also, we have quantitatively found a consistent correlation between the SME and Birkeland current for both summer and winter solstice periods, so that relationship is independent of ionospheric conductivity. This finding is consistent with the idea that the Birkeland currents are closed via the eastward and westward electrojets. The relationship between the current flowing through the polar ionosphere and the F10.7 index for the summer solstice weeks follows the expected pattern. For larger F10.7, hence large ionospheric conductivity, the larger the current for a given solar wind electric field. However, for the winter solstice period, this relationship is reversed, with a larger F10.7 correlated with a smaller net current flowing through the ionosphere. To explain this result, we must consider how the voltage across the polar cap is generated in the first place, and the effect of ionospheric conductivity on that voltage.

The Force Balance Model for the generation of the ionospheric potential due to reconnection explains how ionospheric conductivity controls the portion of the trans-polar potential generated by merging [Lopez et al., 2010]. For identical solar wind conditions, the Region 1 currents are larger for a higher ionospheric conductivity. Larger Region 1 currents cause greater magnetopause erosion [e.g., Wiltberger et al., 2003]. Thus, the magnetopause at noon is closer to the Earth for higher levels of ionospheric conductivity compared to lower levels. This can be seen in simulation results taken from Lopez et al. [2010] and presented in Figure 4 in which the magnetopause was about 0.9 times closer to Earth (about 8 vs. 9 Earth radii) and the ionospheric potential was 0.6 times lower (150 kV versus 250 kV) for the higher con-

ductivity case. Observations have confirmed the relationship between magnetopause erosion using the F10.7 index as a proxy for ionospheric conductivity, with larger F10.7 correlated with a more eroded magnetopause [Němeček et al., 2016].

The magnetosheath plasma flow pattern will be modified by this change of shape of the magnetopause. For the higher ionospheric conductivity case, the magnetosphere is blunter, the stagnation of the flow is greater and less magnetic flux will reach the dayside merging line. In other words, the geoeffective length (the y-extent of the solar wind flow that reaches the merging line) gets smaller. The lower dayside merging rate results in a lower ionospheric potential, which is the sum of the potential due to reconnection and the (smaller) potential due to the viscous interaction [Lopez et al., 2010], as seen in the simulation results. Thus, a system with a larger ionospheric conductivity will have a larger total Region 1 current, but a smaller dayside merging rate and so a smaller total ionospheric potential. Since the Region 1 current in the more conducting ionosphere is larger (despite the smaller total ionospheric potential), the electrojet currents closing the Birkeland currents will also be larger.

Now consider the case in which the baseline ionospheric conductivities are not the same in the the two hemispheres. The hemisphere with the larger conductivity will have the largest Region 1 flowing through it, and it will control the amount of magnetopause erosion and the geoeffective length, which sets the value of the portion of the ionospheric potential due to reconnection. Now consider the situation at solstice. The sunlit hemisphere has the higher conductivity and so it controls the overall value of the potential. If the value of F10.7 is larger than average, the sunlit hemisphere is more conducting than average, the Region 1 current is larger than average and the potential from reconnection is lower than average due to a smaller geoeffective length. Since the potential produced by reconnection must be the same in both hemispheres (because the amount of open flux and the changes in that flux must

be the same in both hemispheres), the potential in both polar caps decreases as F10.7 due to the change in the geoeffective length. In the summer polar cap, the increasing F10.7 corresponds to an increase in ionospheric conductivity and an increase in both the total Birkeland current and the electrojet currents, despite the fact that the ionospheric potential decreases. This leads to the correlations between currents and F10.7 seen in the summer solstice weeks. In the dark polar cap, increasing F10.7 does not increase conductivity because the dark region is not illuminated. Therefore, with an unchanged conductivity but a smaller ionospheric potential, the current in the dark hemisphere is reduced as F10.7 increases. Thus our seemingly contradictory result of the current decreasing in the winter solstice hemisphere with increasing F10.7 is actually a direct consequence of the force balance model prediction of the change in the geoeffective length with increasing conductivity.

## 2.4 Conclusions

We have examined the relationships between the total Birkeland current and the SME index in the northern hemisphere as a function of solar wind electric field, season, and F10.7. In agreement with previous studies, we find that the current flowing regardless of season increases with increasing solar wind electric field (for high solar wind Mach number), and the total current during summer solstice is about 40% larger than the current during winter solstice due to the higher conductivity in the sunlit hemisphere. The relationship between the amount of Birkeland current and the SME index is essentially the same during summer and winter solstice periods. This indicates that the relationship is not dependent on ionospheric conductivity. Instead, the correlations is consistent with current continuity and the Birkeland currents being closed via the auroral electrojets. The relationship between F10.7 and the total

current is consistent with the conductivity hypothesis for the summer solstice periods: larger values of F10.7 (larger ionospheric conductivity) are correlated with larger currents for a given solar wind electric field. This relationship is reversed during winter solstice, with high values of F10.7 being correlated with lower values of current for a given solar wind electric field. This result is a natural consequence of the Force Balance Model for the ionospheric potential and it provides additional strong support for that model.

## Acknowledgments

We gratefully acknowledge the SuperMAG website and the data there provided by SuperMAG collaborators. The SME data can be found at `http://supermag.jhuapl.edu/indices/` for the periods described in the paper. We thank the AMPERE team and the AMPERE Science Center for providing the Iridium derived data products. The AMPERE Birkeland current data can be found at `http://ampere.jhuapl.edu/products/itot/daily.html` for each day at 2-min time resolution. We acknowledge the use of the OMNI data set, which were obtained from CDAWeb using the Space Physics Data Facility(SPDF) `https://cdaweb.gsfc.nasa.gov/pub/data/omni/high_res_omni/monthly_1min/`. We acknowledge the support of the US National Science Foundation (NSF) under Grant No. 1916604. We also acknowledge the support of The National Aeronautics and Space Administration (NASA) under Grant No. 80NSSC20K0606 (The Center for the Unified Study of Interhemispheric Asymmetries (CUSIA)) and Grant No. 80NSSC21K2057.

# CHAPTER 3

## MAGNETOHYDRODYNAMIC MODELS

Magnetohydrodynamics is the study of the dynamics of electrically conducting fluids, such as plasma. In space physics, global MHD codes are used to predict and replicate space weather.

## 3.1 MHD Equations

The governing MHD equations are:

$$\frac{\partial \rho}{\partial t} + \nabla \cdot (\rho \vec{v}) = 0, \tag{3.1}$$

$$\rho \frac{\partial v}{\partial t} + \rho(\vec{v} \cdot \nabla)\vec{v} = \vec{J} \times \vec{B} - \nabla \vec{P}, \tag{3.2}$$

$$\vec{E} + \vec{v} \times \vec{B} = \eta \vec{J} + \frac{1}{ne} \vec{J} \times \vec{B}, \tag{3.3}$$

$$\nabla \times \vec{B} = \mu_0 \vec{J}, \tag{3.4}$$

$$\frac{\partial \vec{B}}{\partial t} = \nabla \times (\vec{v} \times \vec{B} - \frac{1}{ne} \vec{J} \times \vec{B} - \eta \vec{J}), \tag{3.5}$$

$$\nabla \cdot \vec{B} = 0, \tag{3.6}$$

$$\frac{\partial}{\partial t}(P \rho^{-\gamma}) = 0, \tag{3.7}$$

where the symbols have their common usage. MHD models have been known to solve different forms or variations of these equations. This set of equations is derived using several assumptions: (1) the characteristic frequency of any change in the system must be smaller than the ion cyclotron frequency and the characteristic length scale in the system must be longer than the ion gyroradius. (2) the characteristic frequency change is less than the electron-ion collision frequency. A full derivation of the MHD equations with appropriate assumptions can be found in Baumjohann and Treumann 2012. Equation 3.3 (Ohm's law) can also look different considering the appropriate assumptions. Many global MHD codes use a variation of this equation in which either

one of the two terms on the RHS are neglected or the RHS is zero all together. The latter is the case in ideal MHD which results in frozen in flux, where the magnetic field moves with the plasma.

## 3.2 Global MHD for Solar wind-Magnetosphere-Ionosphere

The increased sophistication of global MHD codes has propelled them to the forefront of space weather modeling. MHD codes have been used to model different space weather domains individually as well as the interaction between such domains. Leboeuf et al. [1978] first used a two-dimensional global MHD model to reproduce the Dungey topology for a southward IMF interaction with Earth's magnetosphere. However, two-dimensional models of the magnetosphere were incomplete. Akasofu et al. [1978] makes an argument for the extension of MHD models to include both $B_y$ and $B_z$ variations, thereby requiring these models to be three-dimensional. Shortly after, three-dimensional models was developed by Wu et al. [1981] and Brecht et al. [1981]. Again, but this time in three-dimensions, Leboeuf et al. [1981] was able to reproduce the magnetospheric topology associated with southward IMF. Aside, from solar wind-magnetosphere interactions, Global MHD models have also been used to study the solar corona (e.g., Linker et al. [1999] ).

The space surrounding Earth can be split up into different domains, in which phenomena can be modeled separately or across domains. The main domains are the inner heliosphere, heliosphere, and geospace. The inner hemisphere encompasses the Sun's corona. In this domain sun originating phenomena such as CMEs, coronal hoes, and solar flares can be investigated. The heliosphere is a cavity that is bounded by interstellar medium and encompasses the entire Solar System. Geospace is the near-Earth environment. This region includes Earth's magnetosphere, upper atmosphere

and ionosphere. The geospace environment is of specific interest to this dissertation, as it is where the Sun- Earth interactions take place.

There are several global MHD models that have been used to model the geospace environment (too many to mention here), but for the sake of this dissertation I will focus on the Open Geospace General Circulation Model (OpenGGCM) (Raeder et al. 2009), the Lyon-Fedder-Mobarry model (LFM) (Lyon et al. 2004), the Grand Unified Magnetosphere Ionosphere Coupling Simulation (GUMICS) (Janhunen et al. 2012), and the Space Weather Modeling Framework (SWMF)(Tóth et al. 2005). All of these models are available to the general public online (`https://ccmc.gsfc.nasa.gov`) through the Community Coordinated Modeling Center (CCMC). CCMC provides a "runs-on-request" service where users can run simulations through a prompted interface and once the run is complete the results are then published online to the general scientific community.

These four models have the same general approach in modeling the near-Earth environment. Each of them solve the MHD equations on a grid. In LFM, the grid is non-Cartesian, but has Cartesian topology. Calculations done on the LFM grid uses the finite volume method, which means the differential equations are integrated over the individual cell volumes. Figure 3.1c shows a typical non-Cartesian grid. The boundary of the grid is cylindrical. For Open GGCM, the grid is a stretched-Cartesian grid, which is an orthogonal grid with variable spacing in each of the coordinate directions (Figure3.1b). Both GUMICS and SWMF uses an adaptive grid. Figure 3.1d shows how the adaptive grid resolution becomes more course near Earth. These grids are used in the global magnetosphere (GM) domains. In preliminary study, we ran LFM with different grid resolutions for the first 12 hours of 30 May 2010. We compared the simulated Birkeland current (Figure 3.2).

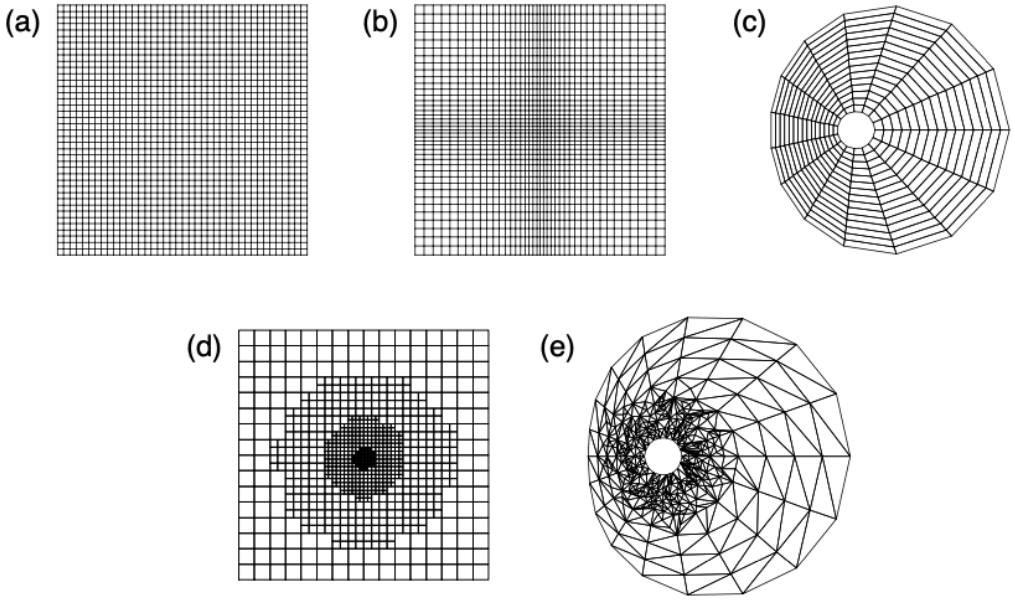


Figure 3.1: From Raeder 2003. Different grids used for global MHD codes. (**a**) shows a typical uniform Cartiesian grid. (**b**) shows a stretched Cartiesian grid. (**c**) is a non-Cartesian grid with Cartesian topology. (**d**) is a structured adaptive grid and (**e**) is an unstructured grid.

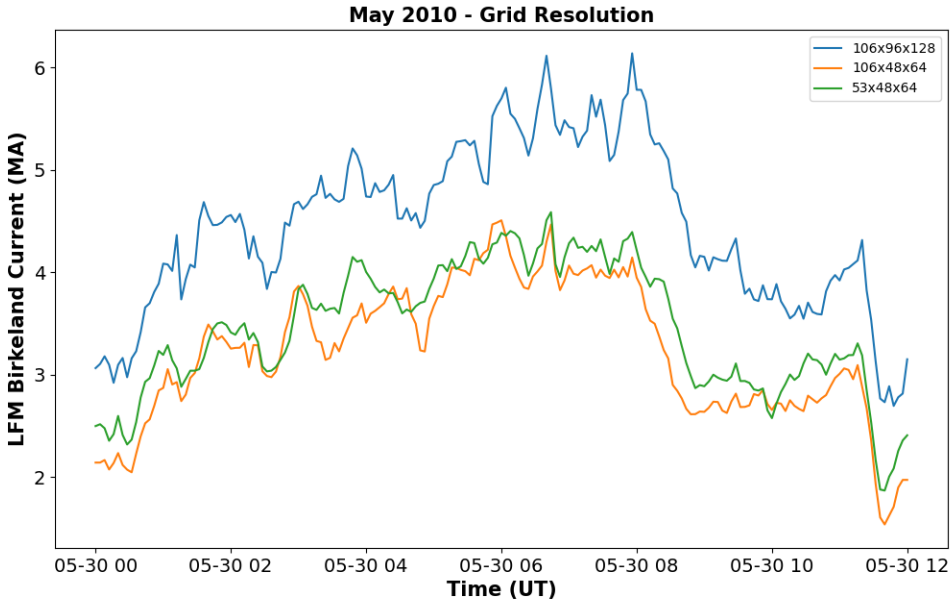


Figure 3.2: Variation in grid resolution for LFM simulation for 2010 May 30 00:00-12:00.

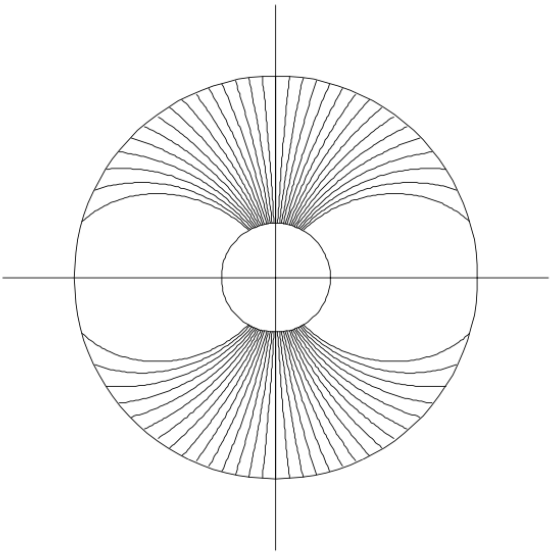

Figure 3.3: From Raeder 2003. Two concentric spherical shells. The outer most shell represents the inner boundary of the magnetosphere. The inner shell represents the ionosphere. The lines between the shells depict the field line mapping of the FACs.

In SWMF, in the GM domain, the resistive MHD equations are solved using the Block-Adaptive-Tree-Solarwind-Roe-Upwind-Scheme (BATS-R-US). BATS-R-US is a MHD code developed at the University of Michigan designed to solve MHD equations using a scheme based on approximate Riemann solvers (Powell et al. 1999).

The boundaries for the GM domain can be different for each model. The upstream boundary (on the dayside) is typically around tens of $R_E$, hundreds of $R_E$ downstream, and about 50-100 $R_E$ orthogonal to the Earth-Sun line. The inner boundary for the MHD grid is approximated by a spherical shell set around 2-3 $R_E$. On this boundary surface, FACs generated in the magnetosphere are then mapped down along field lines to a secondary spherical boundary that marks the ionosphere. Figure 3.3 shows the field line mapping of FACs.

At the ionospheric boundary, a potential equation is solved to determine the ionospheric convection potential:

$$\nabla \cdot \underline{\Sigma} \cdot \Psi = J_{\parallel} sin\delta, \tag{3.8}$$

where $\underline{\Sigma}$ is the conductivity tensor:

$$\underline{\Sigma} = \begin{pmatrix} \Sigma_P/sin^2\delta & -\Sigma_H/sin\delta \\ \Sigma_H/sin\delta & \Sigma_P \end{pmatrix},$$

$\delta$ is the dip angle, $\Sigma_H$ and $\Sigma_P$ are the Hall and Pedersen conductances, respectively, and $\Psi$ is the electrostatic potential. The conductances can be uniform, defined by empirical formulas or computed using an ionosphere-thermosphere model. The conductances are driven by solar EUV irradiation and magnetospheric particle precipitation. The solar EUV driven conductivity is well understood as it is a function of solar irradiation, which is often quantified using the F10.7 flux, and solar zenith angle. The relationships determined by Moen and Brekke 1993 are:

$$\Sigma_H = F_{10.7}^{0.53}(0.81cos\chi + 0.54cos^{1/2}\chi) \tag{3.9}$$

$$\Sigma_P = F_{10.7}^{0.49}(0.34cos\chi + 0.93cos^{1/2}\chi) \tag{3.10}$$

where $F_{10.7}$ is the solar radio flux ( used as a proxy for solar EUV radiation), and $\chi$ is the solar zenith angle. On the other hand, the particle precipitation contribution is much more complicated and is not as well understood. There are several different types of electron precipitation. Newell et al. 2009 defines diffuse, broadband, and monoenergetic precipitation and their role in the global particle precipitation budget. In global MHD codes the precipitating particles are determined by the number flux of electrons in the loss cone and these calculations only account for discrete (i.e., monoenergetic) precipitation. The Robinson formula can be used to compute the Pedersen and Hall conductances (Robinson et al. 1987):

$$\Sigma_P = [40E_0/(16 + E_0^2)]F_E^{1/2} \tag{3.11}$$

$$\Sigma_H = 0.45E_0^{5/8}\Sigma_P \tag{3.12}$$

where $E_0$ and $F_E$ are defined for discrete electron precipitation using the Knight relation (Knight 1973). Once the potential is solved, it is mapped back to the inner magnetosphere boundary where it is used as a boundary condition.

Alternatively the Hall and Pedersen conductances can be calculated using a large-scale ionosphere-thermosphere (IT) model. The MHD model feeds the potential and particle precipitation parameters into the IT model which then computes the conductances self-consistently from the electron-neutral collisions. LMF-MIX with TIE-GCM takes this approach, where the "MIX" portion provides the electric field to the inner boundary condition of the LFM portion and couple to the TIE-GCM portion. It also provides the particle precipitation parameters to TIE-GCM. The TIE-GCM model is a first principle, 3D simulation of the thermosphere-ionosphere system. A more detailed description of this model can be found in Richmond et al. 1992.

To model the ring current electrons, SWMF can use the Rice Convection Model (RCM). RCM calculates the motion of kEV- energy ions and electrons assuming the particles have an isotropic pitch angle distribution (Wolf et al. 1982). In another preliminary study, we investigated the role RCM played in calculating the currents in SWMF. I compared the magnitude of the currents that were determined by SWMF with RCM and SWMF without RCM (Figure 3.4 ) The magnitudes of the Birkeland currents in the SWMF simulation with RCM are larger than those calculated without using RCM, thus the slope for the electrojet-FAC relationship is much lower in the run with RCM. The slope here is much higher than the observational data presented in Figure 2.3 . This is because the observational study's data were hourly average

data from many year. The data presented here is for a much shorter span of time and is not averaged, so the the relationship is magnified.

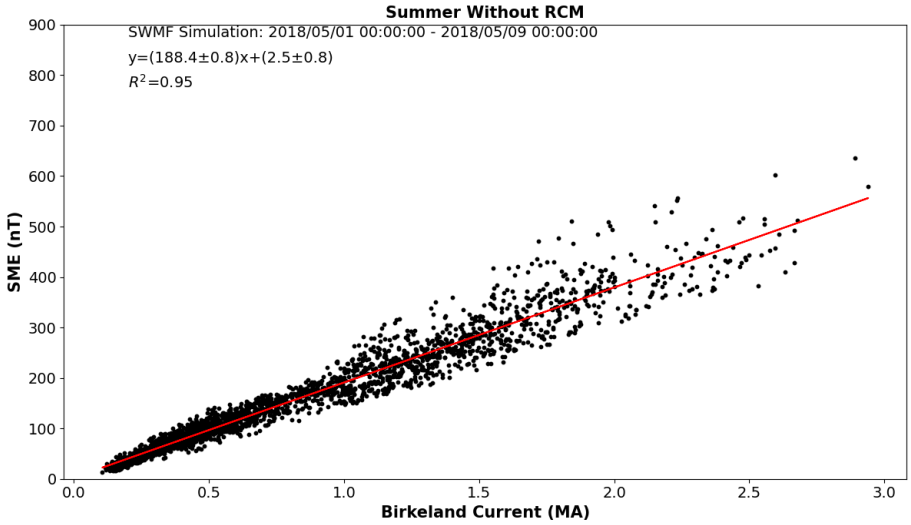


(a)

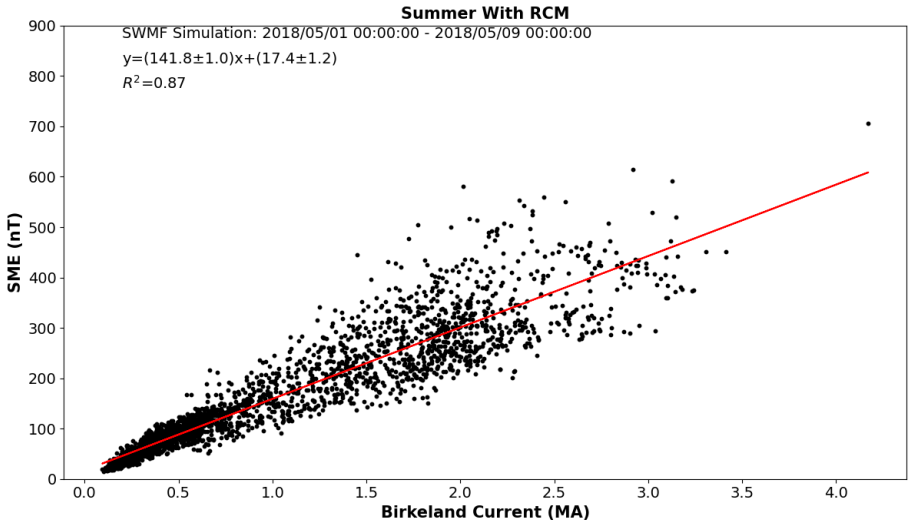


(b)

Figure 3.4: SWMF simulated electrojet - FAC relationship for runs (a) without and (b) RCM.

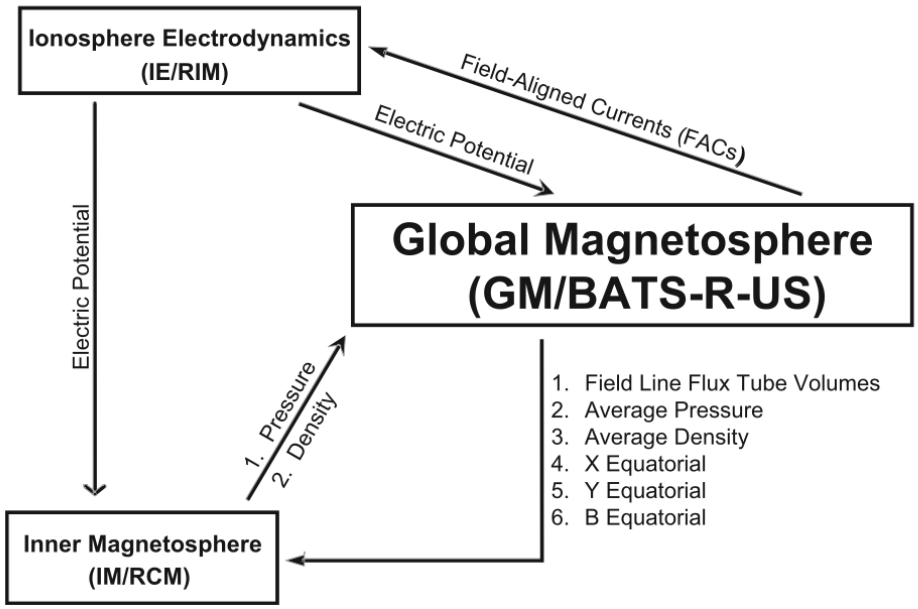


Figure 3.5: Coupling scheme used in SWMF from Zhang et al. [2007].

In SWMF, the ionospheric electrodynamics is approximated using the Ridley Ionosphere Model (RIM) (Ridley and Liemohn 2002, Ridley and Kihn 2004). This model is a 2-D spherical ionospheric potential solver. This model obtains the FACs from BATS-R-US and the upper atmosphere (UA).The UA includes the thermosphere and ionosphere and also provides the Hall and Pedersen conductivities to RIM, if used; else, the conductivities are calculated using the Robinson formula described above. Once the potentials are calculated they are passed to BATS-R-US and RCM. The coupling scheme between these three domains are shown in Figure 3.5 (De Zeeuw et al. 2004,Tóth et al. 2005,Toth et al. 2005).

These global MHD models are used to predict and forecast space weather. So understanding the inner workings of these models and codes is imperative to refining these models' predictive capabilities.

## 3.3 Space Weather Forecasting

The National Oceanic and Atmospheric Administration's (NOAA) Space Weather Prediction Center (SWPC) is the official source of space weather forecasts. SWPC uses global MHD models to forecast space weather phenomena. Depending on the parameter, these models are able to forecast minutes to days.

Though these global MHD models have gained in sophistication, there is still room for improvement. Model validation is necessary to evaluate the current capabilities of these models and to point out their shortcomings. The Geospace Environment Modeling (GEM) is a community-initiated research program dedicated to investigating the dynamics and structure of the geospace environment though the employment of focus groups. These focus groups tackle different space weather dynamics by analyzing observational data and model validation. The latter has been the premise of the GEM modeling challenges. The most recent of these challenges have been done in collaboration with CCMC and Coupling, Energetics and Dynamics of Atmospheric Regions Program (CEDAR).

# CHAPTER 4

## USING OBSERVATION OF IONOSPHERIC CURRENTS TO VALIDATE MODELS

## Quantifying the Ability of Magnetohydrodynamic Models to Reproduce Observed Ionospheric Current Magnitudes

**Coauthors:** Ramon E. Lopez and Alex Glocer

### Citation

James, T., Lopez, R. E., Glocer, A. (2023). Quantifying the Ability of Magnetohydrodynamic Models to Reproduce Observed Ionospheric Current Magnitudes. Manuscript in Preparation.

## SUPPLEMENT

In this work we calculate a SME index from the model output. This calculation is require as it is not a standard SWMF output from the CCMC interface. The calculation of the SME is done using the magnetometer data at ground stations. Although the SME index quantifies the strength of the eastward and westward electrojet in the same way AE does, but with the use of far more stations, the two quantities are, more often than not, dissimilar. In the preliminary work to this study, we look at the discrepancies in the two indices and correlate the electrojet-FAC relationship using both indices. In Figure 4.1a, we present the observational SME and observational AE for the 2015 June 22-24 period. We see that the magnitude of the SME index is larger than the AE. We also present the SWMF derived indices (Figure 4.1b). Again, we see the magnitude of the SME index to be larger than the AE index. At a glance, it seems that in the model the SME index is scaled uniformly. However, there are some instances, in which the same variations in the magnitudes are not seen in both indices. The solar wind data input data for this event is presented in Figure 4.2. Here we can identify these periods in which the variations in SME is very different from the AE to be periods were IMF $B_z$ is strongly southward. These results are in support of the auroral electrojet expanding equatorward during geomagnetic storms, which results in AE underestimating the magnitude of the electrojet.

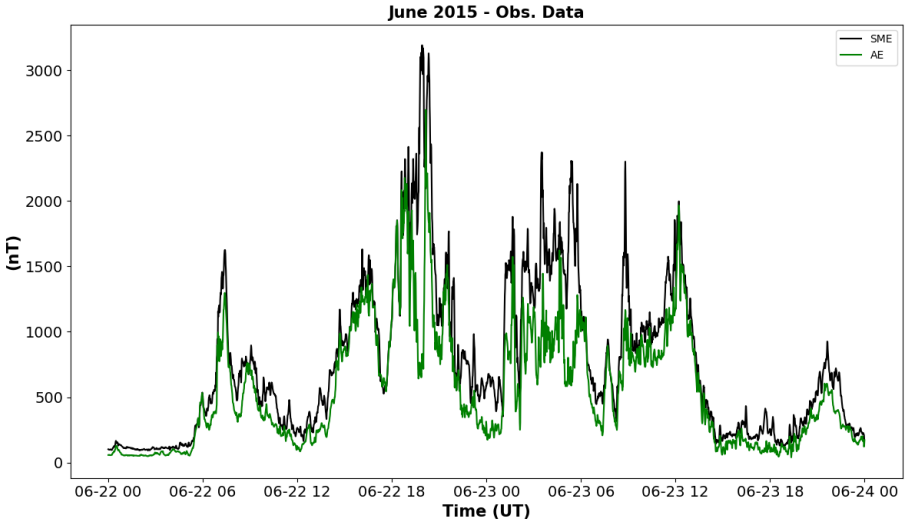


(a)

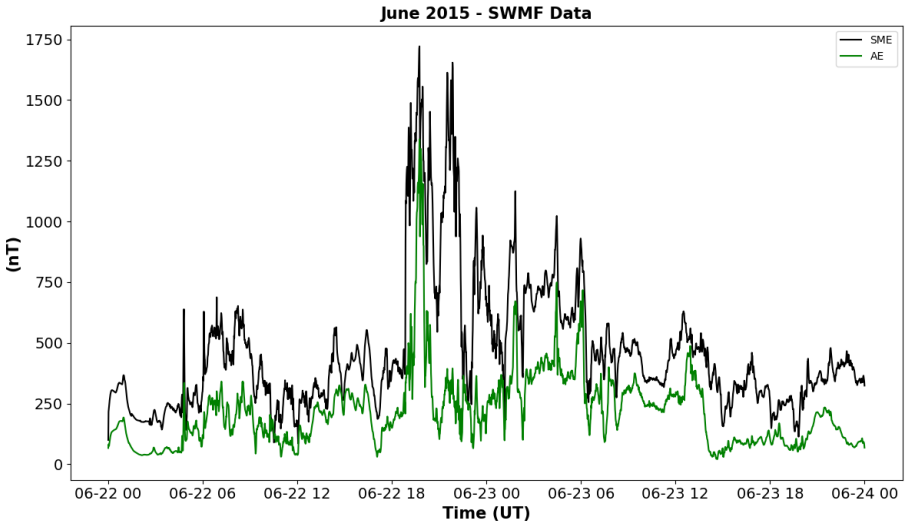


(b)

Figure 4.1: SME and AE indies for 2015 June 22-24 event. Green represents AE and black represents SME.(a) Observational data. (b) SWMF data.

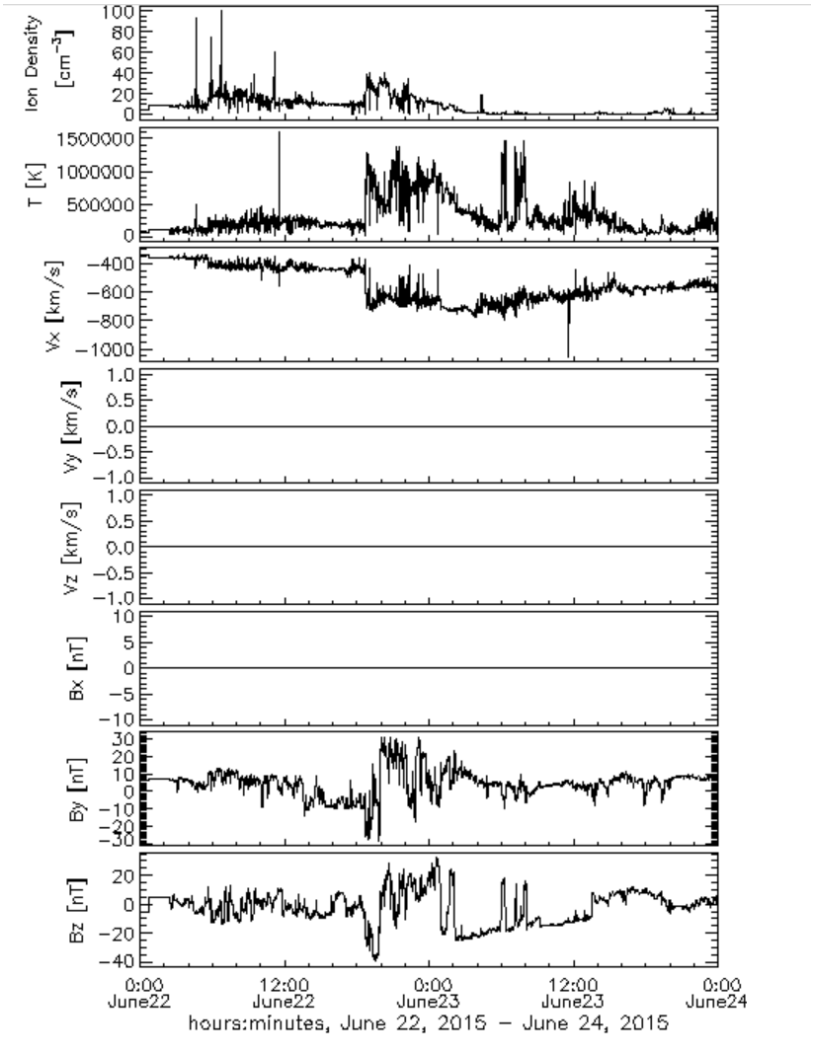


Figure 4.2: OMNI solar wind data. From top to bottom: ion density, temperature, solar wind velocity in the x, y, z directions, and magnetic field in x, y, z directions.

ABSTRACT

Although global magnetohydrodynamic (MHD) models have increased in sophistication and are now at the forefront of modeling Space Weather, there is still no clear understanding of how well these models replicate the observed ionospheric current systems. Without a full understanding and treatment of the ionospheric current systems, global models will have significant shortcomings that will limit their use. In this study we focus on reproducing observed seasonal interhemispheric asymmetry in ionospheric currents using the Space Weather Modeling Framework (SWMF). We find that SWMF does reproduce the linear relationship between the electrojets and the FACs, despite the underestimation of the currents' magnitudes. Quantitatively, we find that at best SWMF is only capturing approximately 60% of the observed current. We also investigate how varying F10.7 effects the ionospheric potential and currents during the summer and winter. We find that simulations ran with higher F10.7 result in lower ionospheric potentials. Additionally, we find that the models do not always replicate the expected behavior of the currents with varying F10.7. This work points to a needed improvement in ionospheric conductance models.

**Keywords:** FAC, SME, MHD, SWMF, F10.7, asymmetry

## 4.1 Introduction

To better understand the dynamics of the interactions that contribute to space weather and to predict their effects, scientists must analyze the underlying physics that contribute, through observations and model validation. As a result of southward interplanetary magnetic field (IMF) merging with the geomagnetic field on the day side, magnetic reconnection occurs on the night side and subsequently transfers

solar wind energy to the magnetosphere and ionosphere (Dungey, 1961). In the ionosphere, the motion of the plasma produced by the solar wind-magnetosphere interaction means that, in the frame of Earth, there is an electric field and voltage across the ionosphere from dawn to dusk. This voltage is directly proportional to the solar wind electric field as long as the solar wind mach number is large (Lopez et al., 2010). However, there are several factors that contribute to interhemispheric asymmetries in this transpolar potential, ionospheric conductivity, density, and more that result from this interaction: different amounts of sunlight, unequal particle precipitation, the offset in the magnetic poles, even different wind patterns (Laundal et al., 2017). Without a full understanding and treatment of these asymmetries, global models will have clear shortcomings that will limit their use. Traditionally, Magnetohydrodynamic (MHD) based global simulations have been at the forefront of modeling the Sun-Earth environment and the dynamics thereof . However, the extent to which these MHD models incorporate and accurately represent interhemispheric asymmetries are unknown. What is known is that these models treat the Northern and Southern hemispheres the same. The domains of these models range from the inner heliosphere to Earth's thermosphere. There are four global magnetosphere MHD-based models are available to the community through the Community Coordinated Modeling Center (CCMC): the Open Geospace General Circulation Model (Open GGCM) (Raeder et al., 2009), the Lyon-Fedder-Mobarry model (LFM) (Lyon et al., 2004), the Grand Unified Magnetosphere Ionosphere Coupling Simulation (GUMICS) (Janhunen et al., 2012), and Space Weather Modeling Framework (SWMF)(Tóth et al. 2005). Though these models are readily accessible, their capabilities to accurately model the global environment and reproduce observations are actively being validated within the space weather community (Gordeev et al., 2015;Mukhopadhyay, 2022;Honkonen et al., 2013). Gordeev et al. 2015 evaluate the four first-principle magnetospheric models ability to replicate

basic magnetospheric global variables realistically, as given by published empirical relationship of these variables. The authors have concluded that these models do a reasonable job at replicating magnetospheric size, magnetic field, and pressure, but there is variation amongst the four models on their performance in predicting the global convection rate, total field-aligned current, and magnetic flux loading into the magnetotail during substorms.

The need for model validation of currents and geomagnetic disturbances has been addressed by community-wide space weather model validation efforts lead by the Geospace Environment Modeling (GEM) Metric and Validation Focus Groups (Pulkkinen et al., 2013;Glocer et al., 2016). However, these studies only looked to validate models at ground magnetometer station locations. We still do not have a comprehensive survey of how well the codes are reproducing observed currents patterns and magnitudes of ionospheric electrojets and Birkeland currents.

Lopez et al. [2022] work focus on the asymmetries in ionospheric conductivity that ultimately controls the amount of current that is allowed to be closed through the conductive ionosphere. During the summer, the northern polar region is tilted towards the sun and therefore receives more sunlight in which in return further ionizes the ionosphere, making it more conductive. However, during the winter, the same polar region is tilted away from the sun, receiving less sunlight, and therefore becomes less conductive. The authors find this rationale to hold qualitatively, using observations. They find there to be larger field-aligned currents flowing into and eastward and westward electrojets in the ionosphere during the summer than during the winter. Secondly, the authors determined the relationship between the electrojets and Birkeland current. Lastly, in investigating the role F10.7 plays in relation to the magnitude of current in the ionosphere, the author's determined that as F10.7 increases during the winter, the magnitude of the currents decreases.

In this work, we quantify the ability of MHD models to reproduce the observed asymmetries in ionospheric currents presented in Lopez et al. [2022].

## 4.2 Methodology

In this section we include a brief description of the Space Weather Modeling Framework (SWMF) and justification for events and data used in this study.

### 4.2.1 Data and Observations

We conduct this study to validate the ability of global MHD models to reproduce ionospheric current magnitudes using observational Birkeland Current data provided by the Active Magnetosphere and Planetary Response Experiment (AMPERE) dataset and observational electrojet strength as quantified by the SuperMag Electrojet index (SME) from the SuperMag dataset. The AMPERE dataset (https://ampere.jhuapl.edu) consists of data from over 66 LEO satellites that are apart of the Iridium constellation. Theses satellites are equipped with magnetometers whose data are then used to make global maps of Birkeland currents(Anderson et al., 2000a; Waters et al., 2001a). The Birkeland current data products are expressed in two-minute increments. The SuperMag data are collected and derived as described in Gjerloev [2012a]. The SuperMag Electrojet index (SME) is used in this study as a measure for the auroral electrojet activity. Typically the AE index is used as a measure of auroral electrojet activity. However, in this study we use the SuperMag Electrojet index (SME). SME is derived in the same way that AE is. However, SME uses over 150 stations while AE uses about 12 stations and thus is a more global measure of the electrojets. The magnitude of the electrojets are indexed by finding the largest northward or southward perturbation from ground magnetometers. AU

or SMU is the largest northward perturbation indicating the largest eastward electrojet. AL or SML is largest southward perturbation indicating the largest westward electrojet and AE or SME is determined by subtracting AL form AU.

The simulated data is provided by SWMF output. We run several SWMF simulations using CCMC's runs-on-request feature. The model output is made publicly available, once the run is finished. AE and Birkeland current are standard output parameters for these runs, in one minute increments. SME, however is not. In this study, the simulated SME is calculated independently using the ground magnetometer data from the models, in the same way the observational SME is derived.

The AMPERE Birkeland current data are provided in two minute intervals, therefore all data sets used in comparison to the observational Birkeland current are averaged every two-minutes.

### 4.2.2 Model Description

The SWMF integrates nine numerical models: the Solar Corona, Solar Eruption Generator, Inner Heliosphere, Solar Energetic Particles, Global Magnetosphere, Inner Magnetosphere, Radiation Belt, Ionospheric Electrodynamics, and Upper Atmosphere & Ionosphere, into one coherent model (Tóth et al., 2005). Each domain or model exchanges information with one another to simulate the real world dynamics of the system interactions. The Global Magnetosphere (GM) includes the planet's bow shock, magnetopause, and magnetotail. The physics of this domain is approximated by solving the resistive MHD equations and using the Block-Adaptive-Tree-Solarwind-Roe-Upwind-Scheme (BATS-R-US). BATS-R-US is typically restricted to the domain $2.5R_E$ from the center of Earth and expands to about $30R_E$ on the dayside, hundreds of $R_E$ on the night side, and $50-100R_E$ in the directions orthogonal to

the Sun-Earth line. The domain inside $2.5R_E$ is approximated by the Inner Magnetosphere (IM), Radiation Belt (RB), and Ionosphere Electrodynamics (IE) components of the SWMF model. In this domain the IM may use the Rice Convection Model (RCM)(Toffoletto et al., 2003; De Zeeuw et al., 2001) to calculate the distribution function of the ring current ions and electrons given an electric and magnetic field distribution. The RCM self consistently computes field-aligned currents and potentials. There are other codes that have been developed to preform similarly (e.g. , the Comprehensive Inner-Magnetosphere Ionosphere (CIMI) Model; Fok et al., 2014).

In the IE component, the Ridley Ionosphere Model (RIM) works as a height averaged electric potential solver, which uses the field-aligned currents from GM and Upper Atmosphere (UA) to calculate particle precipitation and conductances and get a pattern of the electric potential throughout the ionosphere (Ridley and Liemohn, 2002;Ridley and Kihn, 2004). The UA includes the thermosphere and the ionosphere and it extends from around 90km to about 600km altitude for the Earth. The Hall and Pedersen conductives are calculated from the electron density and integrated along field lines and then passed along to the IE component of the model.

The setup of CCMC's runs-on-request feature offers the options to use RCM with or without the Radiation Belt Environment (RBE) when creating a SWMF run. It is important to note the radiation belts do not feed back to the rest of the magnetospheric solutions, as the radiation belts are the far energy tail of the distribution, they do not affect currents in the calculation which are the focus of this study. Therefore this study could include cases with or without RBE with no impact.

### 4.2.3 Event Selection

To investigate whether or not SWMF reproduces current closure in the ionosphere as seen by observations, we select two SWMF runs, readily available on CCMC's website, one during the winter and the other during the summer. The winter run, Flavia_Cardoso_061521_1 , spans 07 December 2016 08:00 - 10 December 2016 14:00. The summer run, YABING_WANG_102319_3, spans 22 June 2015 00:00 - 24 June 2015 00:00. Both events were ran using v20180525 of SWMF with auroral ionospheric conductance and Rice Convection Model (RCM). Hereafter, these events will be referred to as the December 2016 and June 2015 events, respectively.

## 4.3 Findings and Discussion

### 4.3.1 Current Closure

In investigating the capability of SWMF to replicate ionospheric current closure, we compared the currents from the June 2015 and December 2016 events. Just as in Lopez et al. [2022], we have quantified linear relationships between Birkeland current and SuperMag Electrojet (SME) (Figures 4.3 & 4.4). Figure 4.3 shows the observational data and SWMF data for the winter event. The slopes of the two figures are similar to one another and are reasonably close to what is reported by Lopez et al. [2022] (Figure 4.5). The June event also shows a similar slope in both the observational data and the SWMF data (Figure 4.4). It is evident in both figures that the magnitude of the SWMF generated currents are almost half of what was observed for the events.

Figure (4.6) shows the correlation between the generated Birkeland current from SWMF and the observed Birkeland current for both events. Though the correlation coefficient between the simulation current and the observed currents for the December

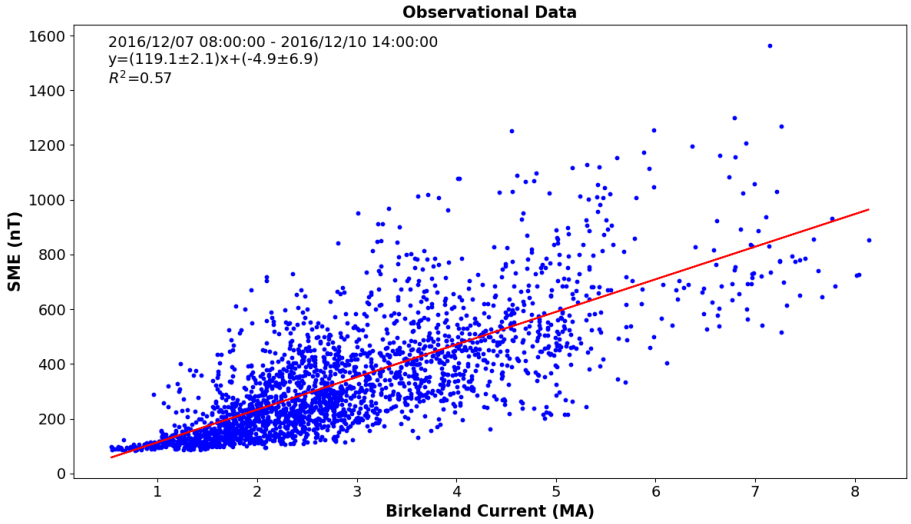


(a)

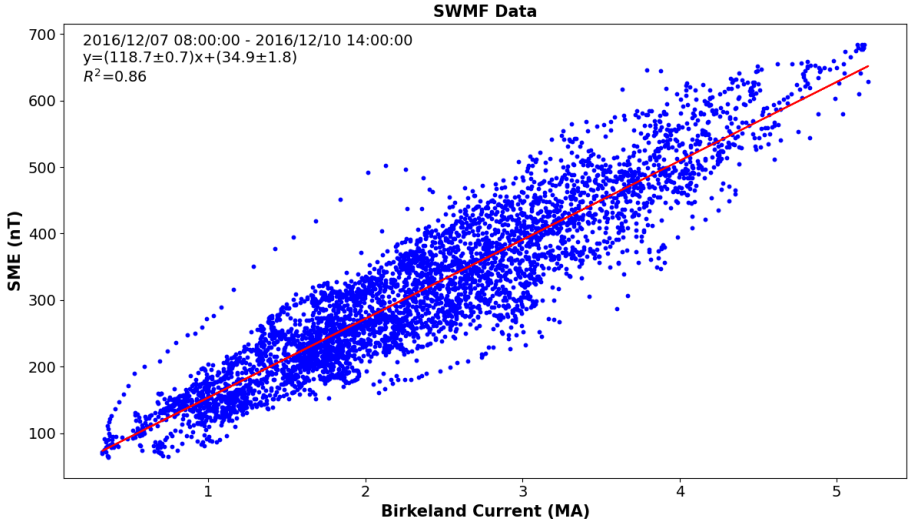


(b)

Figure 4.3: The relationship between SME and total Birkeland Current as determined by observations **(a)** and by SWMF **(b)** for a Winter event.

event is very poor, the current closure relationship for that event is consistent. Despite there being an underestimation of the Birkeland current and even a failure to replicate observations, SWMF is able to reproduce a current closure relationship similar to that presented in Lopez et al. [2022].

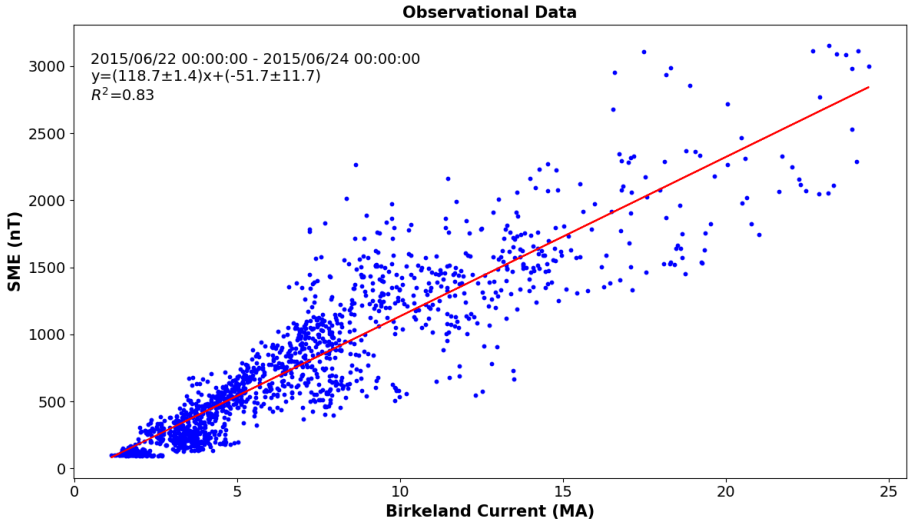


(a)

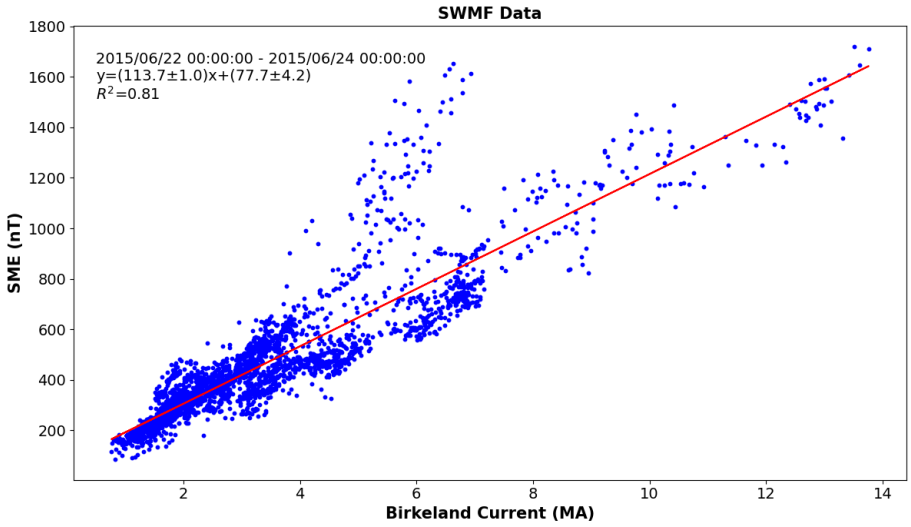


(b)

Figure 4.4: The relationship between SME and total Birkeland Current as determined by observations **(a)** and by SWMF **(b)** for a Summer event.

### 4.3.2 Seasonal Ratio

To examine the seasonal asymmetry between currents we take a look at simulation results from four periods. These periods are: 2011 December 18-25, 2016 December 7-10, 2011 June 18-25, and 2015 June 22-24, days 18-25 of each month.

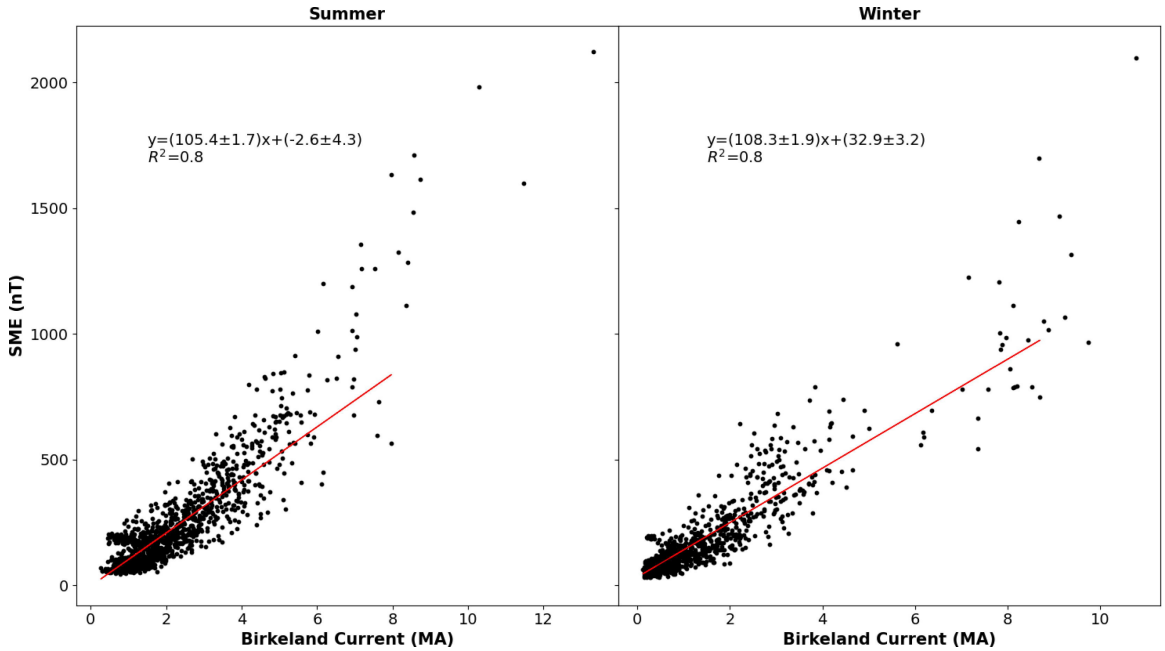


Figure 4.5: Figure from Lopez et al. 2022. Observational data displaying the relationship between the auroral electrojet and field-aligned current for Summer and Winter.

The June 2015 period was driven with data from ACE, the December 1026 period was driven with data from Wind, and the other two periods were driven using the OMNI dataset. For December 2011, the magnitude of the currents in the Southern Hemisphere are larger than the currents in the Northern hemisphere (Figure 4.8). For June 2011 and June 2015, the currents are larger in the Northern Hemisphere (Figures 4.7 & 4.10). These periods reproduce the expected seasonal asymmetry with the sunlit polar region having larger currents. However, for the December 2016 period the simulated currents are larger in the Northern Hemisphere compared to the Southern Hemisphere (Figure 4.9). We would expect the opposite behavior, if we only consider the conductivity resulting from the seasonal asymmetry in solar irradiation. Examining the entire period, the average total simulated Birkeland current was 2.36 MA in the Northern Hemisphere and 2.15 MA in the Southern Hemisphere. The

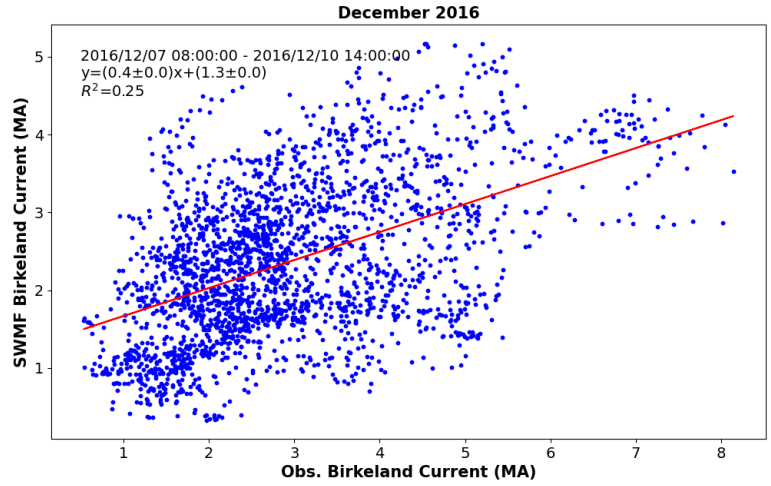


(a)

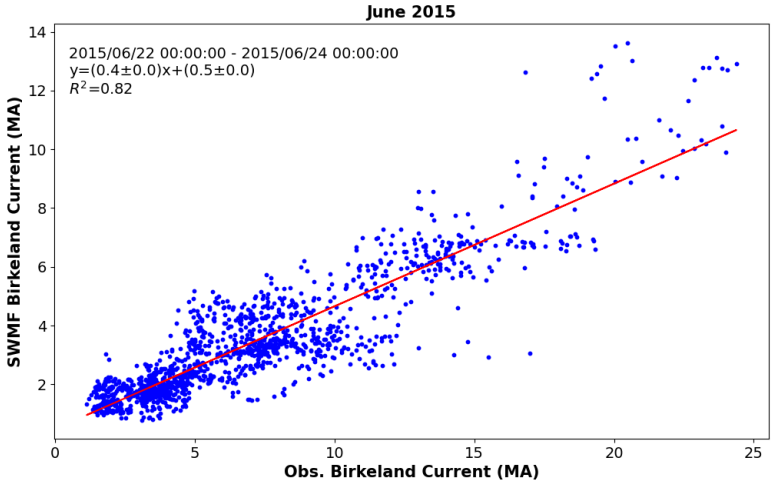


(b)

Figure 4.6: Observations and SWMF Birkeland current for Winter **(a)** and Summer **(b)** Events. The currents for the Summer event is more strongly correlated than those during the Winter event.

AMPERE data had an average total Birkeland current of 2.93 MA in the Northern Hemisphere and 2.68 MA in the Southern Hemisphere. There are two items to note in this comparison. First the interhemispheric asymmetry is the same in both the observations and the simulation. Second, the pattern of the simulated currents being

less than the observed current shows up in the averages. The fact that both the observations and the simulations have an asymmetry opposite to that expected from the asymmetry in the F10.7 flux suggests that this is a real effect. At present, we do not have an explanation for this finding, however, inspecting the AMPERE dataset, we find many examples in winter months of the total Birkeland current in the Northern (dark) Hemisphere being larger than the current in the Southern (sunlit) Hemisphere. On the other hand, we do not find the reverse; it is quite rare is the summer months for the Southern (dark) Hemisphere to have larger total Birkeland current than the current in the Northern (sunlit) Hemisphere. This finding requires significant investigation beyond the scope of this paper to quantify and explain. For all the events the correlation coefficients between the observed and simulated currents are poor and is indicative of the difficulty of SWMF to replicate reality reliably. However, in the previous subsection, we have shown that SWMF's inability to replicate the actual values and variations in the observed currents to have no bearing on how well the model is able to replicate the relationship between the simulated Birkeland current magnitude and simulated SME. From these results, we can say the correlation coefficients are not necessarily an indicator of how well interhemispheric conductivity is being replicated.

### 4.3.3 F10.7 Study

F10.7 is a proxy for the measure of solar irradiation. We expect as F10.7 increases there would also be an increase in the amount of current in the ionosphere. Additionally, we expect as F10.7 increases for the potential across the ionosphere to decrease, as a consequence of the change in geoeffective length (Lopez et al. [2010],

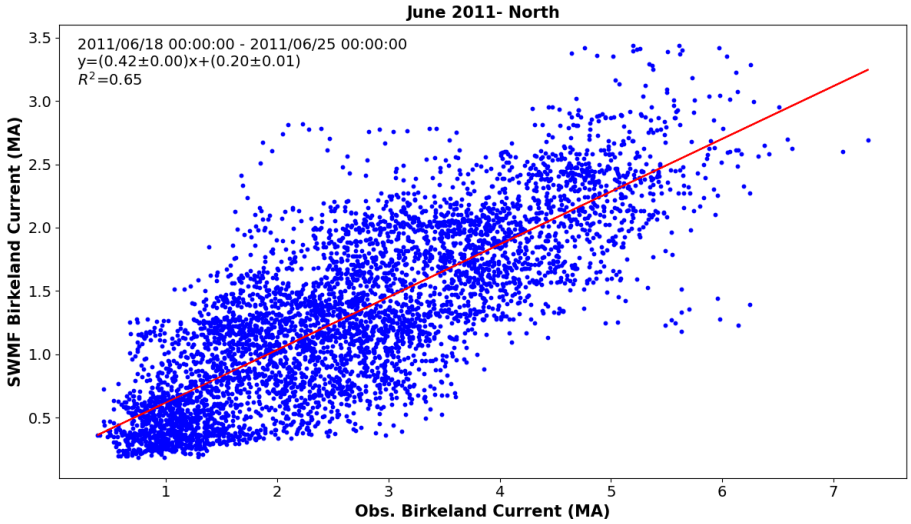


(a)

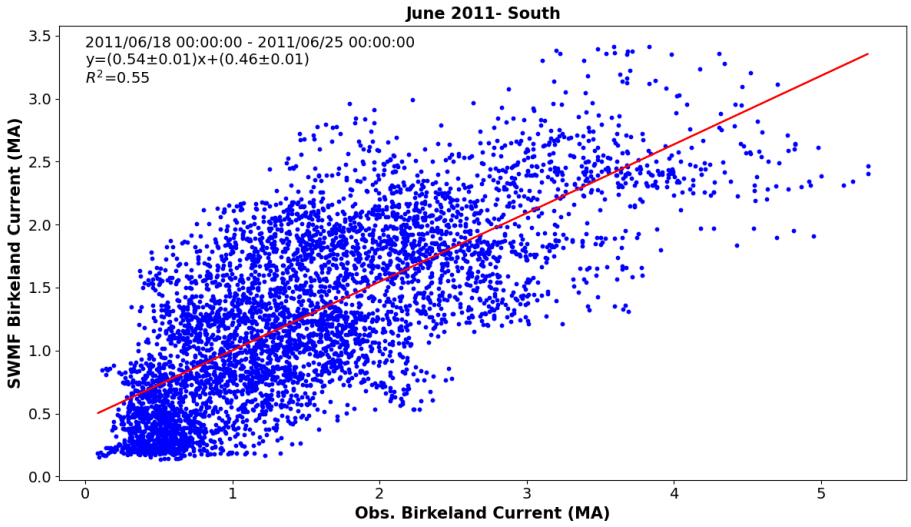


(b)

Figure 4.7: Observations and SWMF Birkeland current for June 2011. **(a)** Northern Hemisphere **(b)** Southern Hemisphere.

consistent with observed F10.7 dependence of the position of the nose of the magnetopause (Němeček et al., 2016).

To examine this question, we consider a 1-week period centered on the winter solstice in December of 2010. For two different runs, we fixed the value of F10.7,

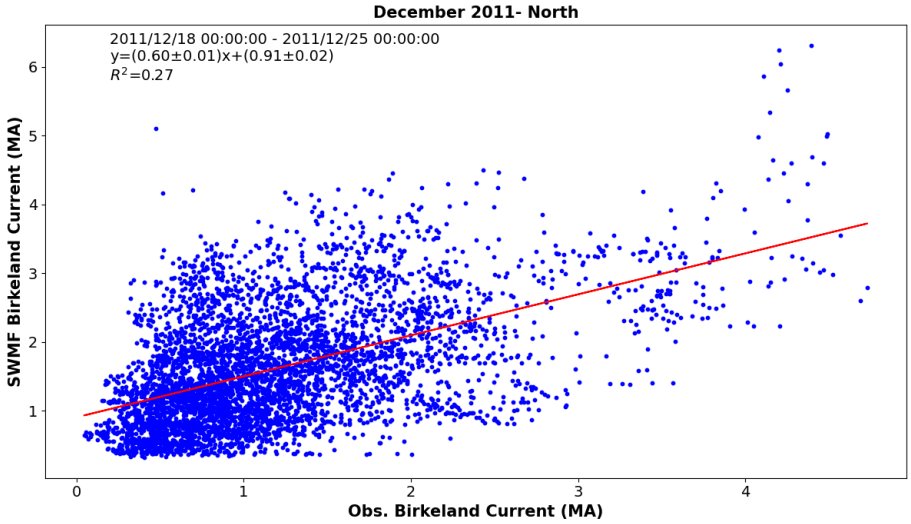


(a)

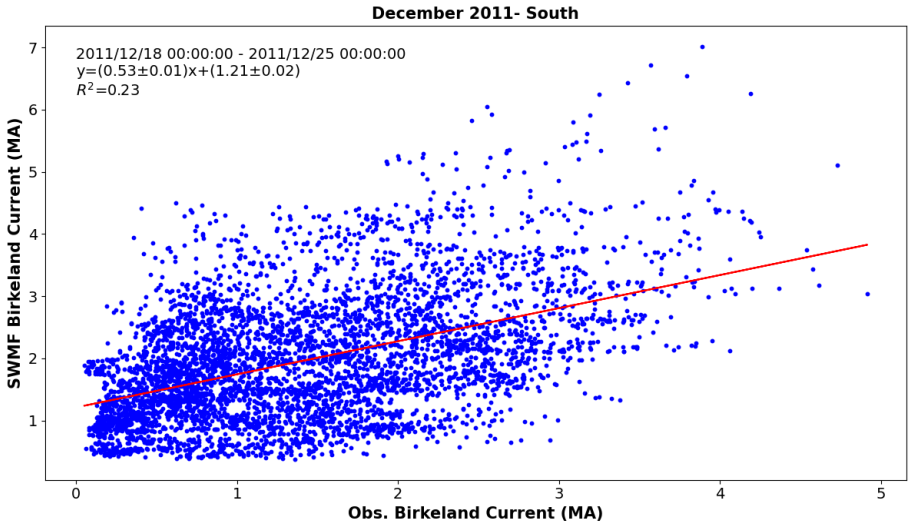


(b)

Figure 4.8: Observations and SWMF Birkeland current for December 2011. **(a)** Northern Hemisphere **(b)** Southern Hemisphere.

then simulated the period using the SWMF driven by the original solar wind time series. One run had a fixed F10.7 of 80 and the other has an F10.7 of 180. We consider F10.7 of 80 to be a reference value for low solar EUV flux and F10.7 of 180 to be a reference high value. We find that as F10.7 increases, the ionospheric

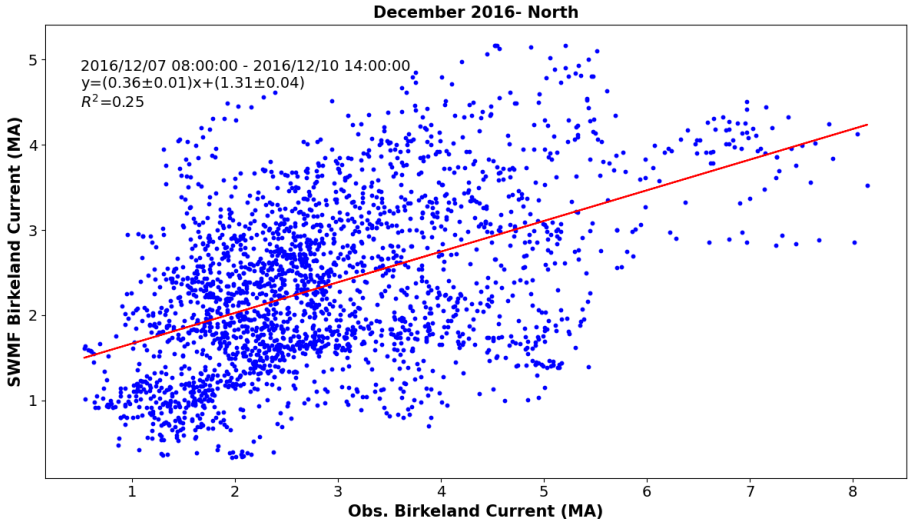


(a)

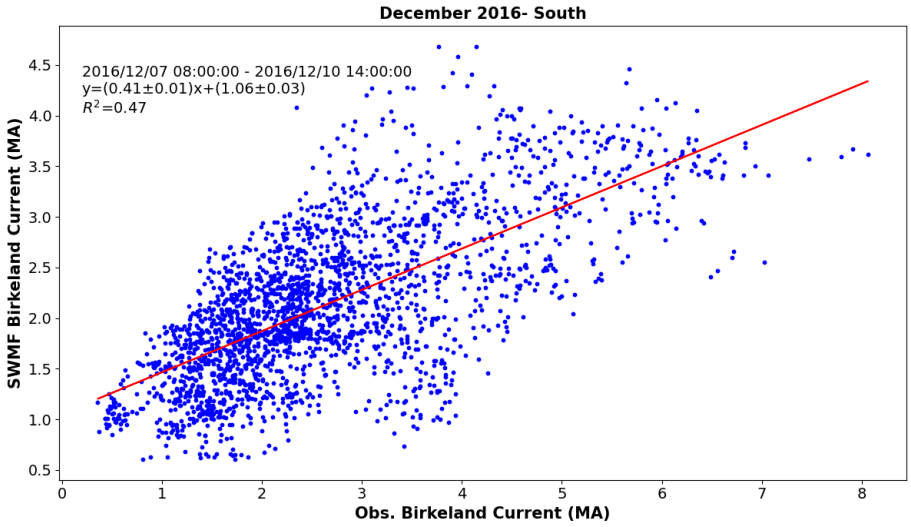


(b)

Figure 4.9: Observations and SWMF Birkeland current for December 2016. **(a)** Northern Hemisphere **(b)** Southern Hemisphere.

potential in both hemispheres decreases, as seen in Figures4.11 & 4.12. This is what is expected (Lopez et al., 2010), that higher conductivity results in a lower ionospheric potential. In contrast to the simulation results for the potential, the average total Birkeland currents for the two runs do not show exactly the same pattern as

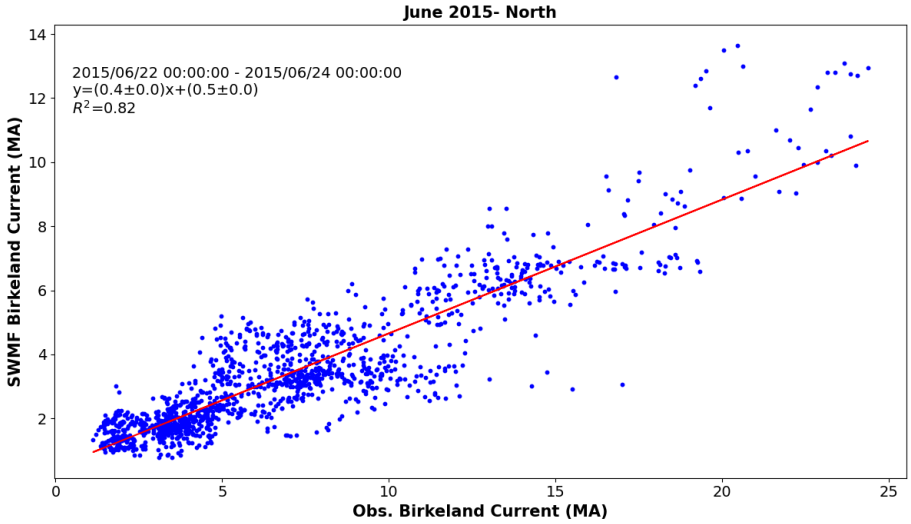


(a)

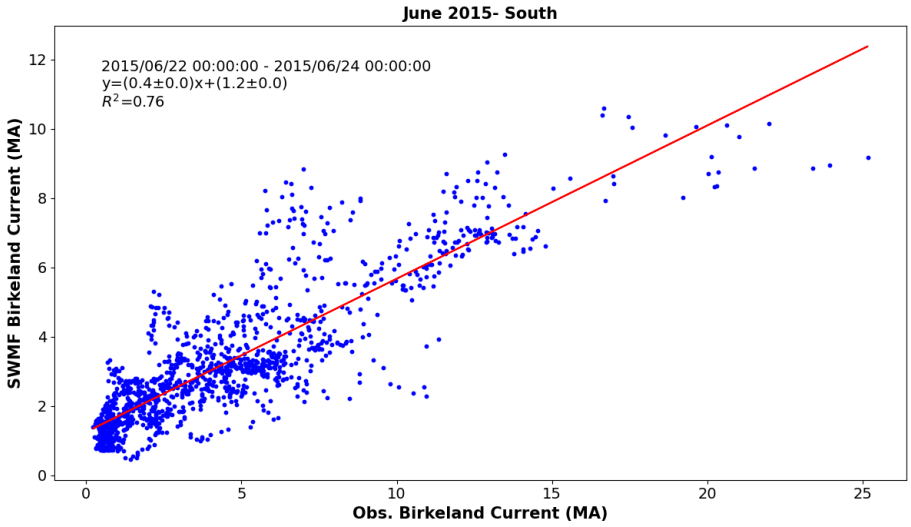


(b)

Figure 4.10: Observations and SWMF Birkeland current for June 2015. **(a)** Northern Hemisphere **(b)** Southern Hemisphere.

determined from observations (Lopez et al., 2022). Table 4.1 presents the average Birkeland current for the two runs in the Northern and Southern Hemispheres. The expected seasonal asymmetry is present in both the low and high F10.7 runs, with the summer (southern) hemisphere having larger average current. However, both

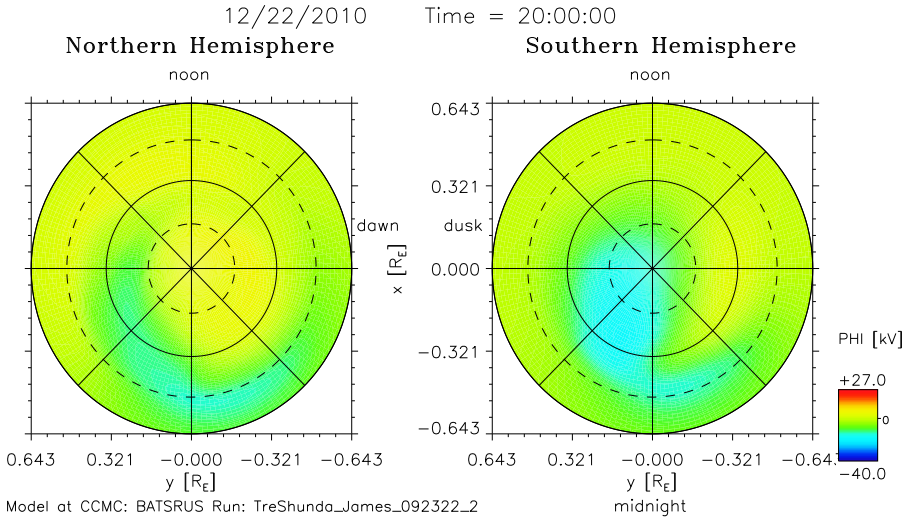


(a)

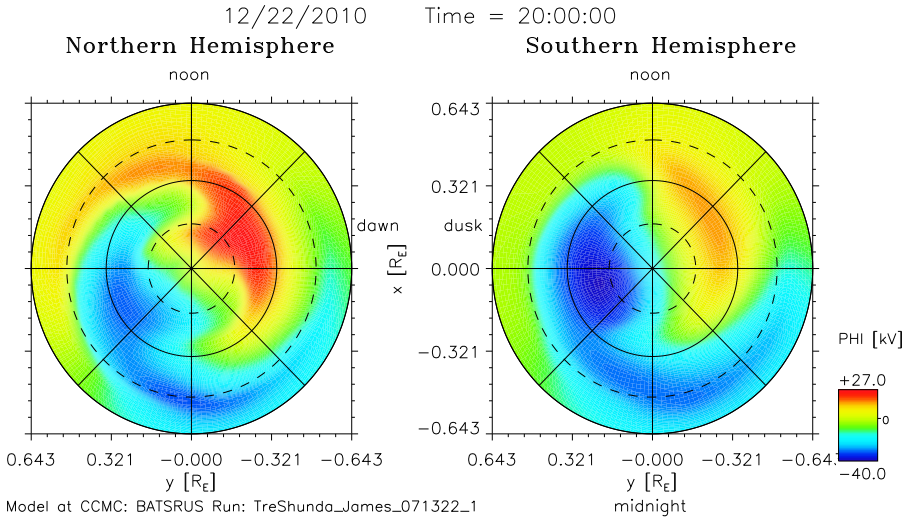


(b)

Figure 4.11: **(a)** Potential map for F10.7 of 180. **(b)** Potential map for F10.7 of 80.

hemispheres had lower average Birkeland current values in the higher F10.7 runs (which also had the lower potentials). Observations show that on average the sunlit (summer) hemisphere has a larger Birkeland current for higher values of F10.7, while the dark (winter) hemisphere has smaller Birkeland current. This was interpreted as being due to the variation in conductance with solar radiation and the unequal amounts of solar EUV conductance in the two hemispheres (Lopez et al., 2022).

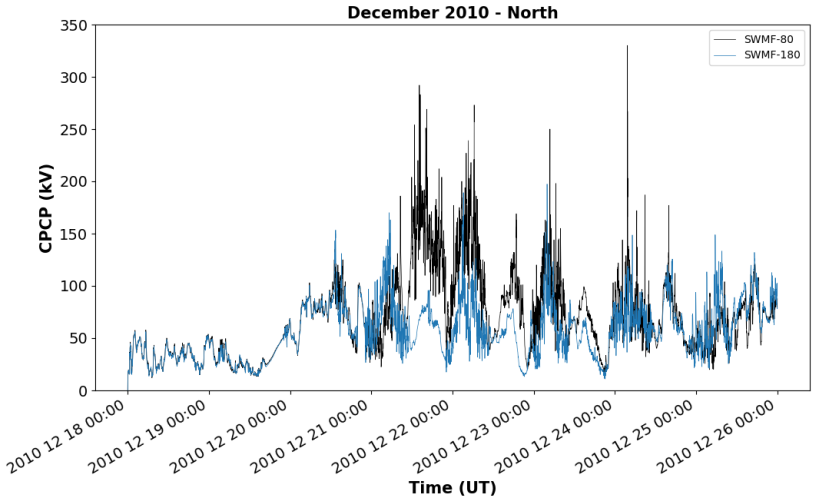


(a)

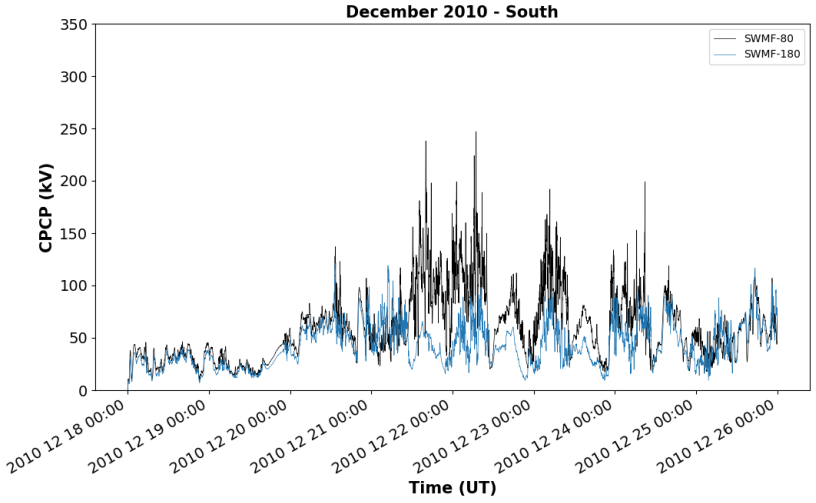


(b)

Figure 4.12: The time series for the SWMF calculated cross polar cap potentials (CPCP) for F10.7 of 80 (black) and 180 (blue). **(a)** Shows the CPCP in the Northern Hemisphere. **(b)** Displays the CPCP in the Southern Hemisphere.

In MHD global models, the Knight Relation is used to get an estimate of electron flux (Knight, 1973) and an empirical relationship is used to calculate the Hall and Pedersen conductances due to precipitating particles (Robinson et al., 1987). This conductance is then added to the solar EUV conductance to determine the overall

| F10.7 [sfu] | Northern Hemisphere [MA] | Southern Hemisphere [MA] |
|---|---|---|
| 80 | 2.36 | 2.84 |
| 180 | 1.99 | 2.55 |

Table 4.1: Average Birkeland current magnitudes with varying F10.7 for SWMF simulation of 2010 December 18-25.

conductivity (Fedder et al., 1995). However, in Wiltberger et al. [2004], the authors conducted a direct comparison and found this traditional calculation of the conductivity to be insufficient, because the MHD model used consistently underestimated the electron precipitation and over-estimated the cross-polar cap potential (CPCP) as compared to observations. In SWMF, rather than using the Knight Relation for the conductivity, this model uses a different empirical relationship. The runs in this study use an empirical relation between the FAC and conductance based on AIMEE data (i.e., the Ridley Legacy Model). A detailed description of this model can be found in Mukhopadhyay et al. 2020.

In fact, inspecting Figure 4.12, one can see that the values of the potential are high, often exceeding 150 KV in both hemispheres for the low F10.7 run. But such large potentials are only observed during geomagnetic storms and for the period simulated the solar wind was very moderate, with southward IMF barely exceeding 5 nT a handful of times and flow speed generally below 400 km/s. Therefore, it is clear that the simulation was producing unrealistically large ionospheric potentials due to an unrealistically low ionospheric conductivity.

## 4.4 Conclusions

We have conducted an investigation of the ability of the SWMF to replicate the observed SME index and the magnitude of the Birkeland currents as observed by AMPERE. We find that for some events, the correlation between the observed

quantities and the simulated quantities are good. However, the simulated Birkeland currents and SME index are generally smaller than the observed quantities during these "good" events. On the other hand, the relationships between the simulated Birkeland current and the simulated SME is quite similar to the same relationship obtained from observations. This is consistent with the interpretation that this relationship is an expression of current closure, with the electrojets closing the Birkeland current system. Moreover, this relationship exists in the simulation data irrespective of the correlation between the simulations and observations for a given event, which also supports this interpretation.

The simulation however, does not always reproduce the seasonal asymmetry in the currents. Observations indicate that the currents are larger in the summer hemisphere, and sometimes this is what the SWMF simulations produce, but not always as can be seen in the December 2016 solstice week, the simulation gives the opposite result. The simulation result for December 2016 is mirrored in the AMPERE data; to understand this apparent anomaly in both simulation and observational results requires additional study. The simulation also replicates the expected variation in the ionospheric potential with F10.7, with larger F10.7 yielding lower ionospheric potentials. However, the simulation do not entirely replicate the behavior of the total Birkeland current seen in observations. We conclude that better models for the ionospheric conductance are required.

## Conflict of Interest Statement

The authors declare that the research was conducted in the absence of any commercial or financial relationships that could be construed as a potential conflict of interest.

## Author Contributions

TJ and RL contributed to conception and design of the study. TJ ran the MHD simulations, unless otherwise indicated in the text. All authors contributed to the analysis of the events studied. TJ wrote the first draft of the manuscript. TJ and RL wrote sections of the manuscript. All authors contributed to manuscript revision, read, and approved the submitted version.

## Funding

We acknowledge the support of the US National Science Foundation (NSF) under Grant No. 1916604. We also acknowledge the support of The National Aeronautics and Space Administration (NASA) under Grant No. 80NSSC20K0606 (The Center for the Unified Study of Interhemispheric Asymmetries (CUSIA)) and Grant No. 80NSSC21K2057.

## Acknowledgments

We gratefully acknowledge the SuperMAG website and the data there provided by SuperMAG collaborators (http://supermag.jhuapl.edu). We thank the AMPERE team and the AMPERE Science Center for providing the Iridium derived data products (http://ampere.jhuapl.edu). Simulation results have been provided by the Community Coordinated Modeling Center at Goddard Space Flight Center through their publicly available simulation services (https://ccmc.gsfc.nasa.gov). We acknowledge use of NASA/GSFC's Space Physics Data Facility's OMNIWeb (or CDAWeb or ftp) service, and OMNI data.

## Data Availability Statement

The datasets and MHD simulation results analyzed in this study can be found in online repositories. The repositories are: http://ampere.jhuapl.edu, http://supermag.jhuapl.edu,https://cdaweb.gsfc.nasa.gov,https://ccmc.gsfc.nasa.gov/results/viewrun.php?domain=GM&runnumber=Flavia_Cardoso_061521_1,https://ccmc.gsfc.nasa.gov/results/viewrun.php?domain=GM&runnumber=YABING_WANG_102319_3,https://ccmc.gsfc.nasa.gov/results/viewrun.php?domain=GM&runnumber=TreShunda_James_071322_1,https://ccmc.gsfc.nasa.gov/results/viewrun.php?domain=GM&runnumber=TreShunda_James_092322_2,https://ccmc.gsfc.nasa.gov/results/viewrun.php?domain=GM&runnumber=TreShunda_James_110222_4, and https://ccmc.gsfc.nasa.gov/results/viewrun.php?domain=GM&runnumber=TreShunda_james_110222_3.

# CHAPTER 5

## CONCLUSIONS & FUTURE WORK

In investigating one of the most significant sources of space weather, ionospheric currents, we conduct a model- observation comparative study. Using observational data, we have quantified the seasonally driven asymmetry in the electrojets and FACs with increasing solar wind electric field. We find the respective ratios, 1.4 and 1.6 to be in agreement with previous studies. We also, for the first time, quantify the relationship between the electrojet, as measure by the SME index, and the FACs. For both winter and summer, the ratio is approximately 110. This is supportive of the present understanding of current continuity– meaning that the FACs that couple the magnetosphere to the ionosphere must be closed by horizontal flowing current in the ionosphere (the electrojets). This is exactly what the linear relationship shown in Figure 3.3 suggests. Additionally, we investigate how the currents behave with increasing F10.7. We find that during the summer, as F10.7 increases so do the electrojets and FACs. This is expected, because solar EUV flux plays a major role in the ionospheric conductivity in which drives the ionospheric currents. Contrasting, during the winter we find that as F10.7 increases, the amount of current decreases. We present the force balance model which explains that the potential due to reconnection in both polar caps decrease as F10.7 increases due to the decrease in geoeffective length. This means that in the dark polar cap, increasing F10.7 with and unchanged conductivity (because it is dark), will actually decrease the magnitude of the currents.

Since global MHD models are used to predict space weather, we investigate the behavior of these ionosphere currents in such models. The governing question here is: to what extent, if at all, do these global MHD models reproduce observational results? To answer this question, we use the SWMF to simulate periods of similar conditions to those from observations. We find that SWMF does reproduce the current-closure relationship, regardless of its underestimation of the currents' magnitudes and even in instances where is does a poor job at replicating reality. Moreover, we find that the models do not always capture the seasonal asymmetry. Even when the ionospheric potential behaves as expected with increasing F10.7, the observed total Birkeland current behavior is not reproduced in the models. There is more work to be done here in regards to resolving the disconnect between the processes done in the model and the physical processes that are occurring in reality.

The results of this work validates the asymmetries in ionospheric currents as seen by observations, provides support for current-closure, quantifies global MHD model's ability to replicate observed ionospheric currents and point to MHD model's shortcomings. There is still work to be done to gain a completely comprehensive understanding of these ionospheric current systems and how well we are able to model them. In the mean time, although these models will continue to be used for space weather predictions, these studies provide support for much needed model improvement.

## 5.1 Future Work

### 5.1.1 More Model Validation

This proposed study will examine MHD models' ability to replicate observed Birkeland currents, on a global and meso-scale. Additionally, this study will also ex-

plore Birkeland currents' relationship to particle precipitation. This three-part study will use the Defense Meteorological Satellite Program (DMSP) and the AMPERE data products to quantify the models' performance. These metrics will be organized in contingency tables and used to calculate skill scores. The results will reveal weaknesses and highlight when and where the models perform best. The same validation and techniques used in this study can also be done with the upcoming GDC mission.

**This study will determine quantitatively how well MHD codes reproduce field-aligned currents (FACs), also known as Birkeland currents, and electrojets' observed magnitudes and distributions. Additionally, as it relates to Birkeland currents, this work will explore the relationship between precipitating particles and FACs.**

By employing quantitative methodologies, this study will determine the type of validation that could be possible with the anticipated Geospace Dynamics Constellation (GDC) data. The timing of this proposal is aligned with the research agenda of GDC to study the magnetosphere- ionosphere-thermosphere (MIT) coupling and dynamics. This proposed course of research could be carried out at NASA's Goddard Space Flight Center's where the current development of the Comprehensive Auroral Precipitation Experiment (CAPE) instrumentation and project science for GDC is being done.

In Wiltberger et al. 2004, the authors conducted a direct comparison and found the traditional calculation of the conductivity ( Chapter 3) to be insufficient, because the MHD model used consistently underestimated the electron precipitation and overestimated the cross-polar cap potential (CPCP) as compared to observations.

In MHD the monoenergetic particle are the only source for precipitating electrons. Khazanov et al. 2021 studies the role of secondary precipitating electrons, which are electrons that result from monoenergetic electrons collisions and escape

back into the magnetosphere and become trapped between the auroral acceleration region and upper atmosphere. Liemohn [2020] points out that these secondary electrons are not accounted for in the Robinson formula and makes a case for the formula's improvement. With an improved particle precipitation calculation, comes improved conductivity calculations, in which improves the determination of FACs and the CPCP. In global MHD models the governing equation that relates conductivity, ionospheric potential, FAC, and horizontal currents flowing in the ionosphere is the current continuity equation:

$$j_R(R1) = [\nabla_\perp \cdot (\Sigma \cdot \nabla\psi)_\perp]_{R=R1} \tag{5.1}$$

where $\Sigma$ is the ionospheric conductance tensor, and $\psi$ is the potential. The right-hand side of the equation represents the FACs and the left-hand side represents the horizontal currents flowing in the ionosphere. This equation is fundamentally a statement of current conservation; currents flowing into the magnetosphere (left hand side), must equal the current closing in the ionosphere (right hand side). Examination of Equation 5.1 shows that, errors in the FAC calculation will directly affect the ionospheric potential as it adjusts to maintain current continuity. Similarly, errors in precipitation will likewise affect the potential and eventually feedback to the magnetosphere and alter the resulting FACs. Moreover, changes in current will also affect the precipitation and hence the conductance. For a global model to accurately capture the electrodynamic interaction between the magnetosphere and ionosphere, it is essential to validate the model's ability to capture FACs as well as the precipitation which drives the conductance.

As it relates to this proposed study, I will be validating the current on the left-hand side, understanding the role particle precipitation plays in the uncertainties that

lie in the ionospheric conductivity tensor that ultimately determines the electrojets on the right-hand side.

The need for model validation of currents and geomagnetic disturbances has been addressed by community-wide space weather model validation efforts lead by GEM Metric and Validation Focus Groups (Pulkkinen et al. 2013, Glocer et al. 2016). However, these studies only looked to validate models at ground magnetometer station locations. We still do not have a comprehensive survey of how well the codes are reproducing observed currents patterns and magnitudes of ionospheric electrojets and Birkeland currents.

In my recent studies, I have used the CCMC run-on-request services to simulate events and quantify MHD models' ability to replicate the observed correlation between the currents in the M-I current system shown in Lopez et al. [2022]. Using SWMF, I have successfully reproduced current-closure between the FAC and the auroral electrojets (Lopez et al. 2022). This is consistent with the FAC being closed by the horizontal ionospheric currents. This proposed research will expand on my existing work by investigating a connection between the global scale and meso-scale structure of FAC. I consider meso-scale to be on the order of 2 degrees in latitude and 1hr local time. My focus will move from the total current system using AMPERE's dataset to untangle the FAC meso-scale structures and compare with particle precipitation data from DMSP. I will use these existing datasets to determine the type of validation that could be possible with the GDC data.

This three-part event-based study will start with investigating total Birkeland current, move to the meso-scale structure of the Birkeland current and finally explore particle precipitation, all while conducting model and observation comparisons. For all parts of the study, I will use a set of events that show a good correlation between AMPERE and SWMF simulated Birkeland current. The simulations are driven by

solar wind input and sometimes the solar wind at Earth can be significantly different than that predicted by OMNI, a data product resulting from propagating solar wind data to the bow shock. If the solar wind input is not a good prediction of reality it can affect the SWMF output. To evaluate the magnitude of the large-scale currents, we want to examine cases where we believe the simulations are replicating reality. The ability of the simulation code to replicate the general behavior of the system and why sometimes the simulation results are different in terms of general variation of observations is not in the scope of this work. I am interested in when simulations are giving a reasonable prediction of reality what are their response to this input and how effective are they at reproducing the actual value of the currents and particle precipitation energy fluxes.

Restricted by AMPERE data availability, these events will span October 2009-June 2022. Characterized using the SME and Dst indices, the events will fall into three different types: quiet times, substorms, and storms. During substorms and magnetic storms, SME experiences an increase due to an enhancement in of energy and momentum transferred from the solar wind resulting from magnetic reconnection. The Dst index measures the ring current, which is indicative of magnetic storms. This data can be found at the World Data Center for Geomagnetism, Kyoto (`https://wdc.kugi.kyoto-u.ac.jp/`). In this study, substorms are events where SME is <500 nT with no ring current developments, storms are events where Dst is < -100 nT, and quiet times are periods where SME is <500 nT.

For each event, I will quantify the relationship between AMPERE and SWMF Birkeland Current, calculating a linear correlation. This analysis will allow me to determine how well SWMF is replicating the magnitudes of observed currents. For example, consider June 22, 2015 00:00:00 - June 24, 2015 00:00:00. With a minimum Dst of -198 nT and a maximum SME of just over 3000 nT, this event is considered

| Forecasts/Observations | Yes | No | Total |
|---|---|---|---|
| Yes | H | F | FY |
| No | M | N | FN |
| Total | OY | ON | T |

Table 5.1: Standard Contingency Table for Dichotomous Forecasts

a storm time event. The correlation coefficient between the total Birkeland currents measured by AMPERE and those calculated using SWMF is 0.82 (Figure 4.10). The slope suggests SMWF is underestimating the total Birkeland current by 40%.

To resolve meso-scale structure of the Birkeland currents, I plan to divide global maps, both from simulations and observations, into bins of 1-hr local time and perform the same correlation mentioned above. Also, for each bin, I will calculate metrics of reaching thresholds and convert these metrics into "yes"/ "no" results to populate a contingency table (Table 5.1). The thresholds will take on incremental values of Birkeland current (e.g., 1 MA, 2 MA, 3 MA, etc.). For each bin, I will evaluate if the SWMF and AMPERE currents exceed the threshold.

In Table 1, for 'H', I will record the number of hours in which SWMF and AMPERE exceeds the set threshold. For 'M', I will record the number of hours SWMF does not exceed the threshold, but the observation does. The number of hours SWMF does exceed the threshold, but the observation does not will be recorded for 'F'. The number of hours that neither SWMF nor AMPERE exceeds the threshold, will be recorded for 'N'. H is the number of hits, M is the number of misses, F is the number of false alarms, and N is the number of correct negatives. FY, FN are the number of forecasted Yeses and Nos, respectively. Likewise, OY and ON are the number of observed Yeses and Nos. From the results of the contingency table, I will conduct statistical calculations (e. g., skill scores) that measures the model's ability to forecast correctly. Additionally, to account for the known strong $B_y$ effects on twisting the

pattern of these global maps in models (Tenfjord et al. 2015), I will rotate the pattern stepping through by 0.5-hr in LT (i.e., 7.5 degrees). For each step, I will calculate the correlation coefficient. I will repeat this process until the offset of data is +/- 6 hrs in LT. I will then find the configuration that provides the maximum correlation coefficient, bin that data by local time, and populate a contingency table using the same reasoning as before. Figure 5.1a shows a map of total Birkeland current from AMPERE for the June 2015 event split into 1hr LT. The current flowing parallel to the magnetic field in the simulation is shown in Figure 5.1b.

The particle precipitation part of this study will utilize DMSP's Special Sensor J (SSJ4/5) data which is an upward-looking instrument measuring precipitating particles from 30 KeV-30 eV with a 1-second cadence (Oberhardt et al. 1994). The SSJ4/5 data is available at `http://cedar.openmadrigal.org`. I will compare SSJ4/5 data with particle precipitation energy flux output from the model. I will also use cross-track magnetic field data from the fluxgate magnetometer (data from the Madrigal site) to identify the location of the Birkeland currents and compare with AMPERE and SWMF output.

Since the SSJ data is calculated along trajectories, I will split the trajectories into 1 minute windows. Depending on the space craft orbit these windows may represent paths through a small change in latitude over a broad local time or vice-versa. In each window, I will evaluate whether the amount of particle precipitation exceeds a threshold for 10 seconds or more. I will consider three thresholds: low, moderate, and strong precipitation, quantified by energy flux. These metrics will then be used to populate a contingency table through the same process previously mentioned. I will also calculate skill scores to further quantify SWMF's ability to replicate SSJ4/5 particle precipitation data.

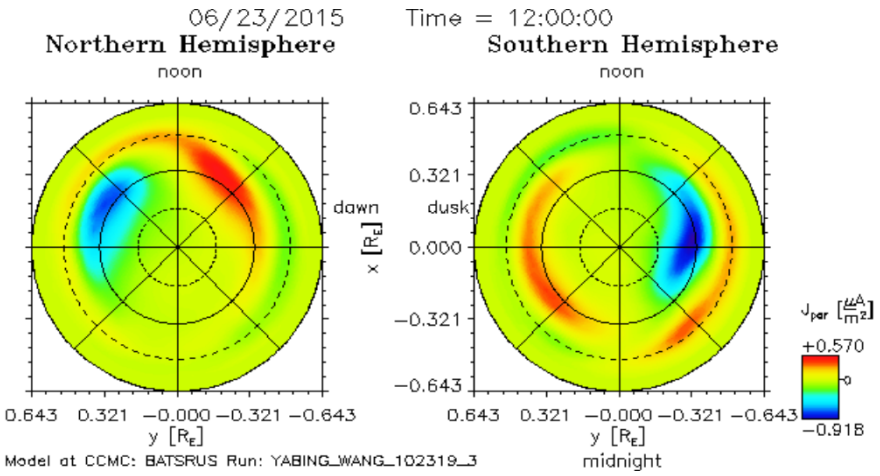


(a)

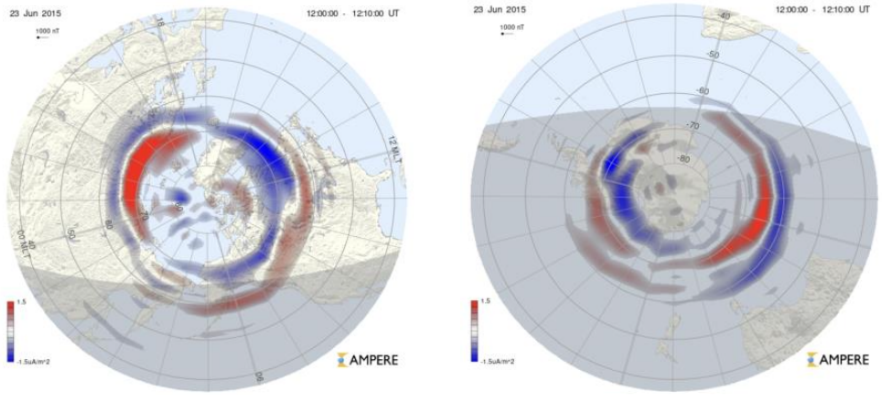


(b)

Figure 5.1: (a)Global maps of the Northern and Southern hemispheres generated by SWMF. (b)Global map of the AMPERE calculated Birkeland current.

It is often easy to say a model is good at forecasting, but exactly what does it mean to be good can be quite vague. Murphy [1993] describes determining the quality, the correspondence between forecasts and observations, as a type of 'goodness.' In his description, the determination of the quality of a model is done be quantifying the correlation between forecasts and observations. Lopez et al. [2007] has used contingency tables to quantify several different models' ability to predict magnetopause crossings as seen by GOES 10 and GOES 12 observations of the Halloween storms.

In a study to evaluate ability of models to predict a local index of magnetic perturbation, Glocer et al. [2016] also used contingency tables and calculated skill scores. To date, no known model validation for Birkeland currents and particle precipitation uses contingency tables and skills scores to quantify the relationship. This study will be the first to determine if SWMF is a 'good' model by way of quantifying its 'goodness' using such methodologies.

From this three-part study, I expect to be able to make conclusive and quantitative statements about how well existing MHD models can reproduce total Birkeland current, meso-scale structure of Birkeland current, and particle precipitation. The contingency table created using the total Birkeland current, should allow me to determine how well MHD models are able to capture reality and the skill score will allow me to further quantify the quality of these models. Because I will be doing this analysis for both the Northern and Southern hemispheres, I may be able to make conclusions about interhemispheric asymmetries. Specifically, I will be able to comment on if the model shows any bias. The ring current model in the SWMF code only couples to the Northern hemisphere, so I expect there to be some interhemispheric conductance effects. I may be able to conclude if the model performs the best during equinox, northern winter, or northern summer. From the meso-scale structure data, I will be able to determine if the models perform better above or below certain magnitudes of Birkeland current.

The additional rotation and rebinning of the data, will also help validate the twisting of the pattern resulting from significant IMF By and I may be able to quantify and correlate the degree of rotation with the magnitude of IMF By. In the particle precipitation analysis, I expect to disentangle the types of precipitation. As the research progresses, I could exclude different types of precipitation from the observations and compare to the model's performance. I expect the implications of

the model validation in this study to help improve the current state of models by quantifying their ability to replicate Birkeland current and precipitating particles in preparation for the upcoming GDC mission.

### 5.1.2 New Electrojet Index (SMP)

In this proposed study, I will investigate instances where there is more or less electrojet than expected for a given amount of Birkeland current. This study will look to answer the following questions:

- How is the electrojet-SME relationship represented during geomagnetic storms?
- Is there a temporal component in these instances? If, so are these instances seen in SWMF simply artifacts of the simulation?
- What role does the Pedersen current play, if any, in the electrojet-FAC relationship?

To conduct this study, I will choose 7-10 geomagnetic storms quantified by Dst indices less than -100 nT. For each event I will determine the electrojet-FAC relationship. Once this relationship is determined, I will compare the value of the slopes to those determined from observational data. Additionally, for each event I will correlate the electrojet-FAC relationship using SWMF and once again compare with observations. In previous studies, I have evaluated SWMF's ability to replicate reality. I plan to do this also, by correlating the SWMF generated Birkeland current with the observed values of the Birkeland current. To investigate temporal features, I will highlight points in 30 minute increments, stepping through by 15 minutes ( i.e., 1-30, 15-45, 30-60, etc. ). I will do this for both the SWMF and observational data. For instances of 30 minutes or more where there is more or less electrojet for a given amount of Birkeland current, I will compare that time period to the respective Dst

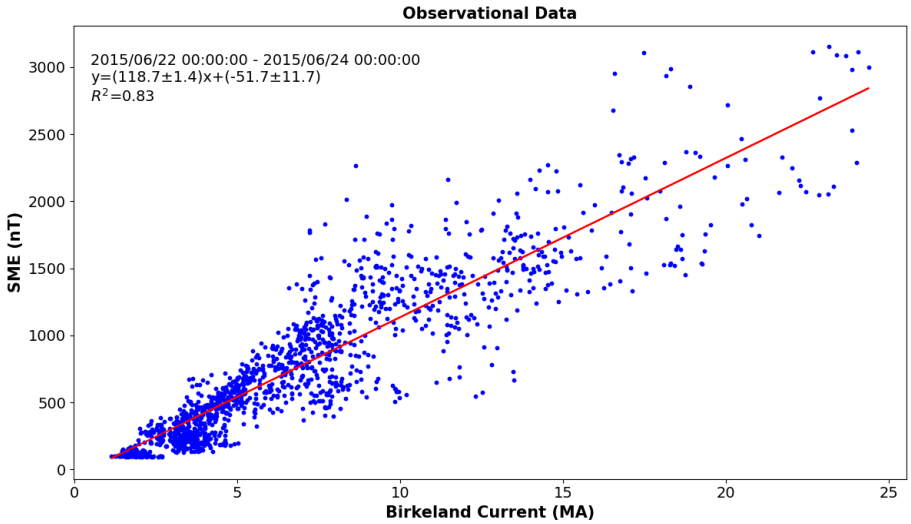


(a)

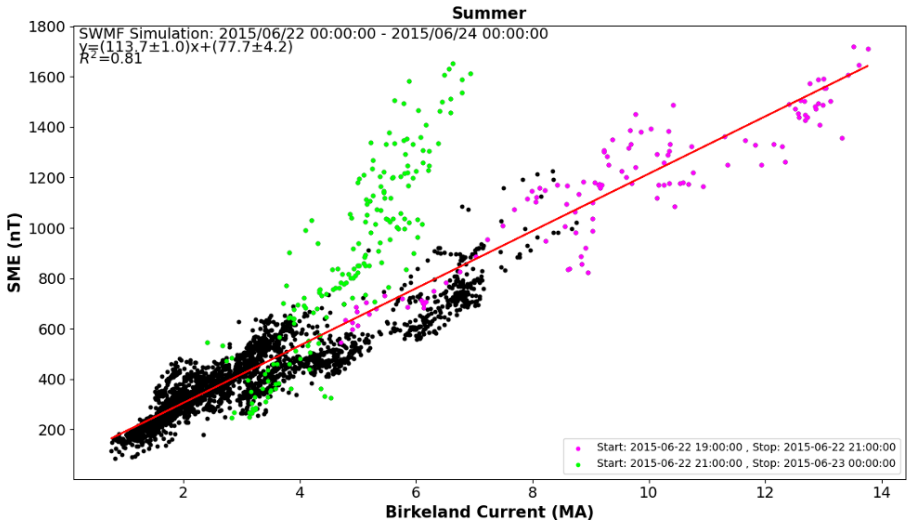


(b) The points correlating with the two hour time period that is representative of the second regime is highlighted in green. The following two hour period is highlighted in magenta.

Figure 5.2: Electrojet - FAC relationship for 2015 June 22-24, (a) Observational data and (b) SWMF simulated data.

data. In doing so, I will be able to determine if these instances are correlated to any specific time period during the storm. For example, does the 30 minute of data where the electrojet is more than expected for a given amount of Birkeland current coincident with the sudden storm commencement, the main phase, or the recovery phase of the storm?

Contrary to the electrojets, the Pedersen current are the north and south flowing current. The SME index is derived from the north and south perturbations in the magnetic field, and thus a similar index can be derived for the Pedersen currents. I have developed, what I will call the SuperMag Pedersen current index (SMP). This index is derived in the same way as SME, but instead of taking the north and south magnetic field perturbations, the east and west magnetic field perturbations are used to determine the north and south flowing current. I will then compare the SME to this new index and look for patterns in which one may dominate over the other.

As an example, I present preliminary findings using the 2015 June 22-24 event from Chapter 4. The observational and simulated electrojet-FAC relationship is presented in Figure 5.2. Both the slopes and correlation coefficients are similar to one another. However, in the SWMF simulation of the event, there is clear second regime of points where there is more electrojet than expected for a given amount of Birkeland current. These two hour period that encompasses the majority of these points is highlighted in green and the following two hour period, highlighted in magenta, falls in a different regime– one in which more tightly hug the line of best fit. This points to there being a temporal component that separates the two regimes.

For this event, I have plotted the simulated Dst data and highlighted the data that corresponds the the periods of interest, using the respective colors (Figure 5.3). The magenta corresponds very well with the main phase of the storm, which is indicative of the ring current build up (Kozyra and Liemohn 2003). The green corresponds

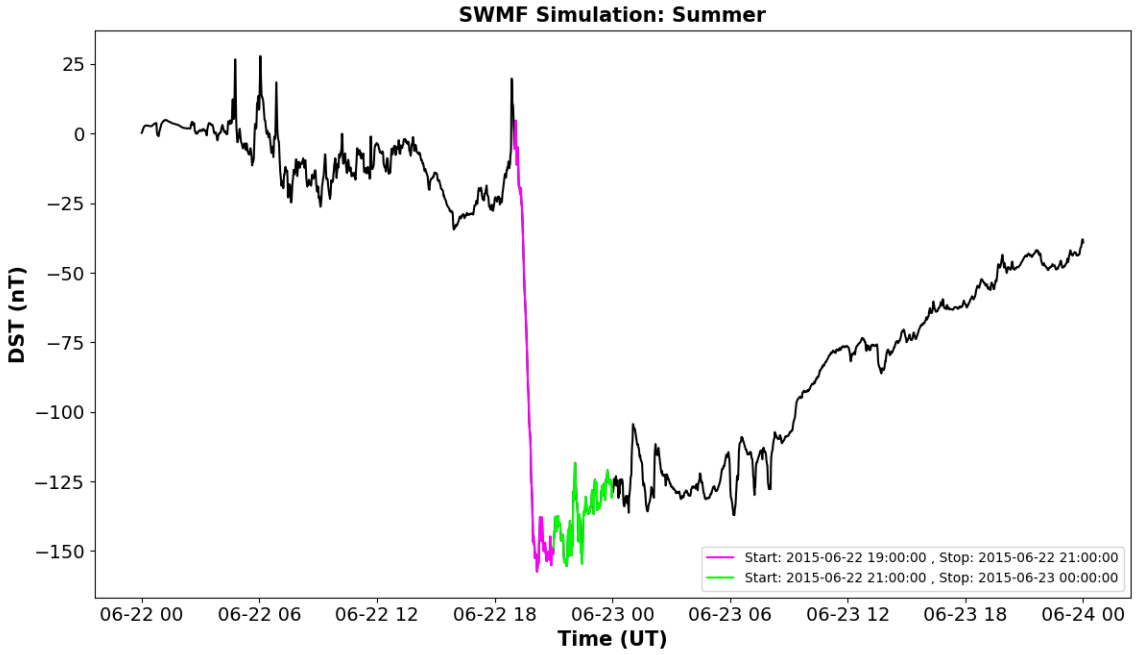


Figure 5.3: Simulated disturbance storm time index for 2015 June 22-24. The color scheme here is the same as indicated in Figure 5.2

.

to the the recovery phase. The ratio of Pedersen current, as represented by SMP, to that of the electrojet is presented as a time series for the event in Figure 5.4. The highlighted region, in green, is that of the second regime. Here the SMP index is much larger than the SME index. However, there are other time periods that exhibit the same behavior but the electrojet-FAC relationship during those times do not deviate much from the expected relationship.

These preliminary results suggest that the second regime of points is an artifact of the simulation, because it does not exists in observations. However, the source and reasoning of the second regime within the code is not completely clear. There is more work to be done here. In regards to the role of the Pedersen current, this too should be investigated in more detail. By analyzing more storm events and comparing to

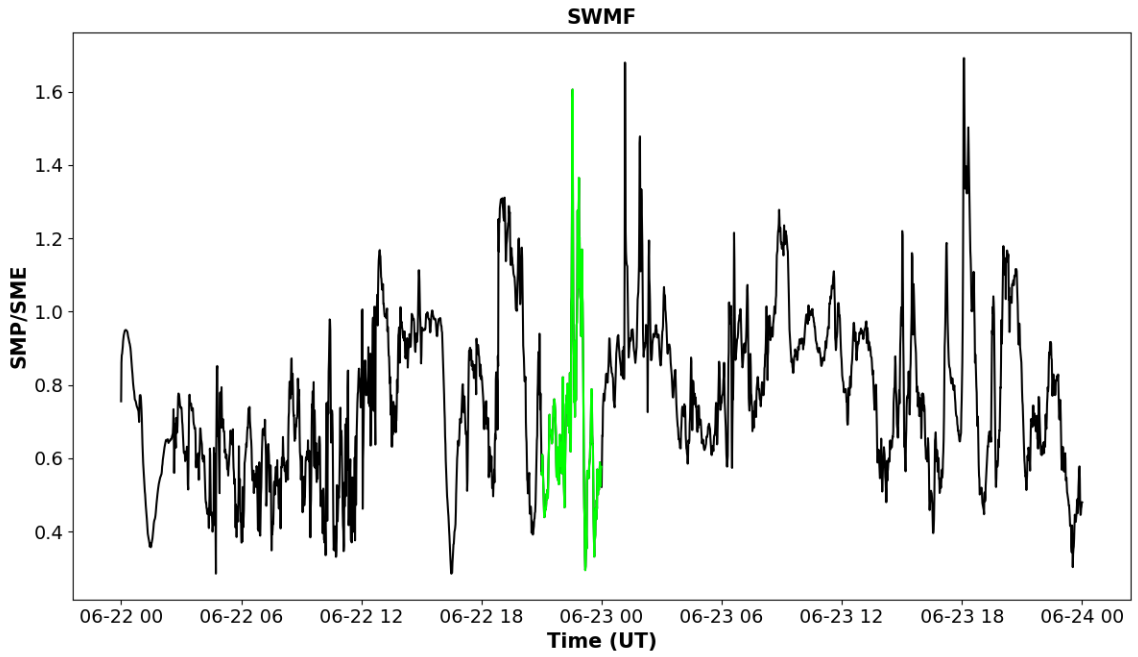


Figure 5.4: The ratio between the Pedersen currents and electrojets for the 2015 June 22-24 event. The color is indicative of the data during the time period of the second regime.

observations, I should be able to resolve a more comprehensive picture of how the models are preforming in replicating observed current during active periods.

Bibliography

S-I Akasofu, ATY Lui, Ching I Meng, and Marion Haurwitz. Need for a three-dimensional analysis of magnetic fields in the magnetotail during substorms. *Geophysical Research Letters*, 5(4):283–286, 1978.

Brian J. Anderson, Kazue Takahashi, and Bruce A. Toth. Sensing global birkeland currents with iridium® engineering magnetometer data. *Geophysical Research Letters*, 27(24):4045–4048, 2000a. doi: https://doi.org/10.1029/2000GL000094. URL `https://agupubs.onlinelibrary.wiley.com/doi/abs/10.1029/2000GL000094`.

Brian J Anderson, Kazue Takahashi, and Bruce A Toth. Sensing global birkeland currents with iridium® engineering magnetometer data. *Geophysical Research Letters*, 27(24):4045–4048, 2000b. URL `https://doi.org/10.1029/2000GL000094`.

W Ian Axford and Colin O Hines. A unifying theory of high-latitude geophysical phenomena and geomagnetic storms. *Canadian Journal of Physics*, 39(10):1433–1464, 1961.

Wolfgang Baumjohann and Rudolf A Treumann. *Basic space plasma physics*. World Scientific, 2012.

Seán P Blake, Antti Pulkkinen, Peter W Schuck, Alex Glocer, and Gabor Tóth. Estimating maximum extent of auroral equatorward boundary using historical and simulated surface magnetic field data. *Journal of Geophysical Research: Space Physics*, 126(2):e2020JA028284, 2021.

Joseph E Borovsky and Joachim Birn. The solar wind electric field does not control the dayside reconnection rate. *Journal of Geophysical Research: Space Physics*, 119 (2):751–760, 2014. URL https://doi.org/10.1002/2013JA019193.

CB Boyle, PH Reiff, and MR Hairston. Empirical polar cap potentials. *Journal of Geophysical Research: Space Physics*, 102(A1):111–125, 1997.

SH Brecht, J Lyon, JA Fedder, and K Hain. A simulation study of east-west imf effects on the magnetosphere. *Geophysical Research Letters*, 8(4):397–400, 1981.

A Brekke and Y Kamide. On the relationship between joule and frictional heating in the polar ionosphere. *Journal of Atmospheric and Terrestrial Physics*, 58(1-4): 139–143, 1996.

R Bruntz, RE Lopez, M Wiltberger, and JG Lyon. Investigation of the viscous potential using an mhd simulation. *Journal of Geophysical Research: Space Physics*, 117(A3), 2012. URL https://doi.org/10.1029/2011JA017022.

Richard C Carrington. Description of a singular appearance seen in the sun on september 1, 1859. *Monthly Notices of the Royal Astronomical Society, Vol. 20, p. 13-15*, 20:13–15, 1859.

Guang-ming Chen, Jiyao Xu, Wenbin Wang, Jiuhou Lei, and Alan G Burns. A comparison of the effects of cir-and cme-induced geomagnetic activity on thermospheric densities and spacecraft orbits: Case studies. *Journal of Geophysical Research: Space Physics*, 117(A8), 2012.

JC Coxon, Stephen E Milan, LBN Clausen, BJ Anderson, and H Korth. A superposed epoch analysis of the regions 1 and 2 birkeland currents observed by ampere during

substorms. *Journal of Geophysical Research: Space Physics*, 119(12):9834–9846, 2014.

Tong Dang, Xiaolei Li, Bingxian Luo, Ruoxi Li, Binzheng Zhang, Kevin Pham, Dexin Ren, Xuetao Chen, Jiuhou Lei, and Yuming Wang. Unveiling the space weather during the starlink satellites destruction event on 4 february 2022. *Space Weather*, 20(8):e2022SW003152, 2022. doi: https://doi.org/10.1029/2022SW003152. URL `https://agupubs.onlinelibrary.wiley.com/doi/abs/10.1029/2022SW003152`. e2022SW003152 2022SW003152.

T Neil Davis and Masahisa Sugiura. Auroral electrojet activity index ae and its universal time variations. *Journal of Geophysical Research*, 71(3):785–801, 1966. URL `https://doi.org/10.1029/JZ071i003p00785`.

D De Zeeuw, S Sazykin, A Ridley, G Toth, T Gombosi, K Powell, and D Wolf. Inner magnetosphere simulations-coupling the michigan mhd model with the rice convection model. In *AGU Fall Meeting Abstracts*, volume 2001, pages SM42A–0830, 2001.

Darren L De Zeeuw, Stanislav Sazykin, Richard A Wolf, Tamas I Gombosi, Aaron J Ridley, and Gabor Tóth. Coupling of a global mhd code and an inner magnetospheric model: Initial results. *Journal of Geophysical Research: Space Physics*, 109 (A12), 2004.

James W Dungey. Interplanetary magnetic field and the auroral zones. *Physical Review Letters*, 6(2):47, 1961.

GM Erickson and RA Wolf. Is steady convection possible in the earth's magnetotail? *Geophysical Research Letters*, 7(11):897–900, 1980.

EA Eroshenko, AV Belov, D Boteler, SP Gaidash, SL Lobkov, R Pirjola, and L Trichtchenko. Effects of strong geomagnetic storms on northern railways in russia. *Advances in Space Research*, 46(9):1102–1110, 2010.

Joel A Fedder, Steve P Slinker, John G Lyon, and RD Elphinstone. Global numerical simulation of the growth phase and the expansion onset for a substorm observed by viking. *Journal of Geophysical Research: Space Physics*, 100(A10):19083–19093, 1995.

M.-C. Fok, N. Y. Buzulukova, S.-H. Chen, A. Glocer, T. Nagai, P. Valek, and J. D. Perez. The comprehensive inner magnetosphere-ionosphere model. *Journal of Geophysical Research: Space Physics*, 119(9):7522–7540, 2014. doi: https://doi.org/10.1002/2014JA020239. URL `https://agupubs.onlinelibrary.wiley.com/doi/abs/10.1002/2014JA020239`.

M Förster and S Haaland. Interhemispheric differences in ionospheric convection: Cluster edi observations revisited. *Journal of Geophysical Research: Space Physics*, 120(7):5805–5823, 2015.

Matthias Förster and Ingrid Cnossen. Upper atmosphere differences between northern and southern high latitudes: The role of magnetic field asymmetry. *Journal of Geophysical Research: Space Physics*, 118(9):5951–5966, 2013.

Ryoichi Fujii and Takesi Iijima. Control of the ionospheric conductivities on large-scale birkeland current intensities under geomagnetic quiet conditions. *Journal of Geophysical Research: Space Physics*, 92(A5):4505–4513, 1987. URL `https://doi.org/10.1029/JA092iA05p04505`.

N Yu Ganushkina, MW Liemohn, and S Dubyagin. Current systems in the earth's magnetosphere. *Reviews of Geophysics*, 56(2):309–332, 2018. URL https://doi.org/10.1002/2017RG000590.

J. W. Gjerloev. The supermag data processing technique. *Journal of Geophysical Research: Space Physics*, 117(A9), 2012a. doi: https://doi.org/10.1029/2012JA017683. URL https://agupubs.onlinelibrary.wiley.com/doi/abs/10.1029/2012JA017683.

JW Gjerloev. The supermag data processing technique. *Journal of Geophysical Research: Space Physics*, 117(A9), 2012b. URL https://doi.org/10.1029/2012JA017683.

A Glocer, L Rastätter, M Kuznetsova, A Pulkkinen, HJ Singer, C Balch, D Weimer, D Welling, M Wiltberger, J Raeder, et al. Community-wide validation of geospace model local k-index predictions to support model transition to operations. *Space Weather*, 14(7):469–480, 2016.

E Gordeev, V Sergeev, I Honkonen, M Kuznetsova, L Rastätter, M Palmroth, P Janhunen, G Tóth, J Lyon, and M Wiltberger. Assessing the performance of community-available global mhd models using key system parameters and empirical relationships. *Space Weather*, 13(12):868–884, 2015.

MR Hairston, TW Hill, and RA Heelis. Observed saturation of the ionospheric polar cap potential during the 31 march 2001 storm. *Geophysical Research Letters*, 30 (6), 2003.

Mike Hapgood, Huixin Liu, and Noé Lugaz. Spacex—sailing close to the space weather?, 2022.

Richard Hodgson. On a curious appearance seen in the sun. *Monthly Notices of the Royal Astronomical Society*, 20:15–16, 1859.

I Honkonen, L Rastätter, A Grocott, A Pulkkinen, M Palmroth, Joachim Raeder, AJ Ridley, and M Wiltberger. On the performance of global magnetohydrodynamic models in the earth's magnetosphere. *Space Weather*, 11(5):313–326, 2013.

Takesi Iijima and Thomas A Potemra. Field-aligned currents in the dayside cusp observed by triad. *Journal of Geophysical Research*, 81(34):5971–5979, 1976. URL https://doi.org/10.1029/JA081i034p05971.

P Janhunen, Minna Palmroth, Tiera Laitinen, I Honkonen, L Juusola, G Facskó, and Tuija I Pulkkinen. The gumics-4 global mhd magnetosphere–ionosphere coupling simulation. *Journal of Atmospheric and Solar-Terrestrial Physics*, 80:48–59, 2012.

Liisa Juusola, Kirsti Kauristie, Olaf Amm, and Patricia Ritter. Statistical dependence of auroral ionospheric currents on solar wind and geomagnetic parameters from 5 years of champ satellite data. In *Annales geophysicae*, volume 27, pages 1005–1017. Copernicus GmbH, 2009. URL https://doi.org/10.5194/angeo-27-1005-2009.

George V Khazanov, Alex Glocer, and Mike Chu. Electron energy interplay in the geomagnetic trap below the auroral acceleration region. *Journal of Geophysical Research: Space Physics*, 126(5):e2020JA028811, 2021.

Stephen Knight. Parallel electric fields. *Planetary and Space Science*, 21(5):741–750, 1973.

Janet U Kozyra and Michael W Liemohn. Ring current energy input and decay. *Magnetospheric Imaging—the Image Prime Mission*, pages 105–131, 2003.

Karl Magnus Laundal, Ingrid Cnossen, Stephen E Milan, SE Haaland, John Coxon, NM Pedatella, Matthias Förster, and Jone Peter Reistad. North–south asymmetries in earth's magnetic field: Effects on high-latitude geospace. *Space Science Reviews*, 206:225–257, 2017.

Benoit Lavraud and Joseph E Borovsky. Altered solar wind-magnetosphere interaction at low mach numbers: Coronal mass ejections. *Journal of Geophysical Research: Space Physics*, 113(A9), 2008. URL `https://doi.org/10.1029/2008JA013192`.

G Le, JA Slavin, and RJ Strangeway. Space technology 5 observations of the imbalance of regions 1 and 2 field-aligned currents and its implication to the cross-polar cap pedersen currents. *Journal of Geophysical Research: Space Physics*, 115(A7), 2010.

JN Leboeuf, T Tajima, Co F Kennel, and JM Dawson. Global simulation of the time-dependent magnetosphere. *Geophysical Research Letters*, 5(7):609–612, 1978.

JN Leboeuf, T Tajima, CF Kennel, and JM Dawson. Global simulations of the three-dimensional magnetosphere. *Geophysical Research Letters*, 8(3):257–260, 1981.

Michael W Liemohn. The case for improving the robinson formulas. *Journal of Geophysical Research: Space Physics*, 125(10):e2020JA028332, 2020.

Jon A Linker, Z Mikić, Doug A Biesecker, Robert J Forsyth, Sarah E Gibson, Alan J Lazarus, A Lecinski, Pete Riley, Adam Szabo, and Barbara J Thompson. Magnetohydrodynamic modeling of the solar corona during whole sun month. *Journal of Geophysical Research: Space Physics*, 104(A5):9809–9830, 1999.

Ramon E Lopez. The integrated dayside merging rate is controlled primarily by the solar wind. *Journal of Geophysical Research: Space Physics*, 121(5):4435–4445, 2016. URL https://doi.org/10.1002/2016JA022556.

Ramon E Lopez et al. The effect of f10. 7 on interhemispheric differences in ionospheric current during solstices. *Advances in Space Research*, 69(8):2951–2956, 2022.

RE Lopez, S Hernandez, Michael Wiltberger, C-L Huang, EL Kepko, H Spence, CC Goodrich, and JG Lyon. Predicting magnetopause crossings at geosynchronous orbit during the halloween storms. *Space Weather*, 5(1), 2007.

RE Lopez, R Bruntz, EJ Mitchell, M Wiltberger, JG Lyon, and VG Merkin. Role of magnetosheath force balance in regulating the dayside reconnection potential. *Journal of Geophysical Research: Space Physics*, 115(A12), 2010. URL https://doi.org/10.1029/2009JA014597.

JG Lyon, JA Fedder, and CM Mobarry. The lyon–fedder–mobarry (lfm) global mhd magnetospheric simulation code. *Journal of Atmospheric and Solar-Terrestrial Physics*, 66(15-16):1333–1350, 2004.

M. McHarg, F. Chun, D. Knipp, G. Lu, B. Emery, and A. Ridley. High-latitude joule heating response to imf inputs. *Journal of Geophysical Research: Space Physics*, 110 (A8), 2005. doi: https://doi.org/10.1029/2004JA010949. URL https://agupubs.onlinelibrary.wiley.com/doi/abs/10.1029/2004JA010949.

Robert L McPherron. Growth phase of magnetospheric substorms. *Journal of Geophysical Research*, 75(28):5592–5599, 1970.

Robert L McPherron. Magnetospheric substorms. *Reviews of Geophysics*, 17(4): 657–681, 1979.

Robert L McPherron, Tung-Shin Hsu, and Xiangning Chu. An optimum solar wind coupling function for the al index. *Journal of Geophysical Research: Space Physics*, 120(4):2494–2515, 2015. URL https://doi.org/10.1002/2014JA020619.

Jøran Moen and Asgeir Brekke. The solar flux influence on quiet time conductances in the auroral ionosphere. *Geophysical Research Letters*, 20(10):971–974, 1993. doi: https://doi.org/10.1029/92GL02109. URL https://agupubs.onlinelibrary.wiley.com/doi/abs/10.1029/92GL02109.

Agnit Mukhopadhyay. Statistical comparison of magnetopause distances and cpcp estimation by global mhd models. *Authorea Preprints*, 2022.

Agnit Mukhopadhyay, Daniel T Welling, Michael W Liemohn, Aaron J Ridley, Shibaji Chakraborty, and Brian J Anderson. Conductance model for extreme events: Impact of auroral conductance on space weather forecasts. *Space Weather*, 18(11): e2020SW002551, 2020.

Allan H Murphy. What is a good forecast? an essay on the nature of goodness in weather forecasting. *Weather and forecasting*, 8(2):281–293, 1993.

Z Němeček, J Šafránková, RE Lopez, Š Dušík, L Nouzák, L Přech, J Šimnek, and J-H Shue. Solar cycle variations of magnetopause locations. *Advances in Space Research*, 58(2):240–248, 2016. URL https://doi.org/10.1016/j.asr.2015.10.012.

Patrick T Newell, Thomas Sotirelis, Kan Liou, and FJ Rich. Pairs of solar wind-magnetosphere coupling functions: Combining a merging term with a viscous term works best. *Journal of Geophysical Research: Space Physics*, 113(A4), 2008. URL https://doi.org/10.1029/2007JA012825.

Patrick T Newell, Kan Liou, and Gordon R Wilson. Polar cap particle precipitation and aurora: Review and commentary. *Journal of atmospheric and solar-terrestrial physics*, 71(2):199–215, 2009.

MR Oberhardt, DA Hardy, WE Slutter, JO McGarity, DJ Sperry, AW Everest, AC Huber, JA Pantazis, and M Pl Gough. The shuttle potential and return electron experiment (spree). *Il Nuovo Cimento C*, 17:67–83, 1994.

S Ohtani, G Ueno, and T Higuchi. Comparison of large-scale field-aligned currents under sunlit and dark ionospheric conditions. *Journal of Geophysical Research: Space Physics*, 110(A9), 2005. URL `https://doi.org/10.1029/2005JA011057`.

Shinichi Ohtani, Jesper W Gjerloev, Magnar Gullikstad Johnsen, Masatoshi Yamauchi, Urban Brändström, and Andrew Marc Lewis. Solar illumination dependence of the auroral electrojet intensity: Interplay between the solar zenith angle and dipole tilt. *Journal of Geophysical Research: Space Physics*, 124(8):6636–6653, 2019. URL `https://doi.org/10.1029/2019JA026707`.

Vladimir O Papitashvili and Frederick J Rich. High-latitude ionospheric convection models derived from defense meteorological satellite program ion drift observations and parameterized by the interplanetary magnetic field strength and direction. *Journal of Geophysical Research: Space Physics*, 107(A8):SIA–17, 2002.

VO Papitashvili, Freddy Christiansen, and Torsten Neubert. A new model of field-aligned currents derived from high-precision satellite magnetic field data. *Geophysical Research Letters*, 29(14):28–1, 2002. URL `https://doi.org/10.1029/2001GL014207`.

ED Pettigrew, SG Shepherd, and JM Ruohoniemi. Climatological patterns of high-latitude convection in the northern and southern hemispheres: Dipole tilt depen-

dencies and interhemispheric comparisons. *Journal of Geophysical Research: Space Physics*, 115(A7), 2010.

R Pirjola, A Viljanen, A Pulkkinen, and O Amm. Space weather risk in power systems and pipelines. *Physics and Chemistry of the Earth, Part C: Solar, Terrestrial & Planetary Science*, 25(4):333–337, 2000.

Kenneth G Powell, Philip L Roe, Timur J Linde, Tamas I Gombosi, and Darren L De Zeeuw. A solution-adaptive upwind scheme for ideal magnetohydrodynamics. *Journal of Computational Physics*, 154(2):284–309, 1999.

George B Prescott. *History, theory, and practice of the electric telegraph*. BoD–Books on Demand, 2022.

A Pulkkinen, L Rastätter, M Kuznetsova, H Singer, C Balch, D Weimer, G Toth, A Ridley, T Gombosi, Michael Wiltberger, et al. Community-wide validation of geospace model ground magnetic field perturbation predictions to support model transition to operations. *Space Weather*, 11(6):369–385, 2013.

Antti Pulkkinen, E Bernabeu, A Thomson, A Viljanen, R Pirjola, D Boteler, J Eichner, PJ Cilliers, D Welling, NP Savani, et al. Geomagnetically induced currents: Science, engineering, and applications readiness. *Space Weather*, 15(7):828–856, 2017.

Joachim Raeder. Global magnetohydrodynamics-a tutorial. *LECTURE NOTES IN PHYSICS-NEW YORK THEN BERLIN-*, pages 212–246, 2003.

Joachim Raeder, Douglas Larson, Wenhui Li, Emil L Kepko, and Timothy Fuller-Rowell. Openggcm simulations for the themis mission. *The THEMIS Mission*, pages 535–555, 2009.

Patricia H Reiff and Janet G Luhmann. Solar wind control of the polar cap voltage. *Solar wind magnetosphere coupling*, 126:453, 1986.

AD Richmond, EC Ridley, and RG Roble. A thermosphere/ionosphere general circulation model with coupled electrodynamics. *Geophysical Research Letters*, 19(6): 601–604, 1992.

AJ Ridley and EA Kihn. Polar cap index comparisons with amie cross polar cap potential, electric field, and polar cap area. *Geophysical research letters*, 31(7), 2004.

AJ Ridley and MW Liemohn. A model-derived storm time asymmetric ring current driven electric field description. *Journal of Geophysical Research: Space Physics*, 107(A8):SMP–2, 2002.

AJ Ridley, Tamas I Gombosi, and DL DeZeeuw. Ionospheric control of the magnetosphere: Conductance. In *Annales Geophysicae*, volume 22, pages 567–584. Copernicus GmbH, 2004. URL `https://doi.org/10.5194/angeo-22-567-2004`.

RM Robinson, RR Vondrak, K Miller, T Dabbs, and D Hardy. On calculating ionospheric conductances from the flux and energy of precipitating electrons. *Journal of Geophysical Research: Space Physics*, 92(A3):2565–2569, 1987.

JM Ruohoniemi and RA Greenwald. Dependencies of high-latitude plasma convection: Consideration of interplanetary magnetic field, seasonal, and universal time factors in statistical patterns. *Journal of Geophysical Research: Space Physics*, 110 (A9), 2005.

David G Sibeck, RE Lopez, and Edmond C Roelof. Solar wind control of the magnetopause shape, location, and motion. *Journal of Geophysical Research: Space Physics*, 96(A4):5489–5495, 1991.

M Sugiura and T Kamei. Equatorial dst index 1957–1986, iaga bull., 40. *Berthelier and M. Menville (Int. Serv. Geomagn. Indices Publ. Off., Saint Maur, 1991)*, 1991.

K. F. Tapping. The 10.7cm solar radio flux (f10.7). *Space Weather*, 11(7):394–406, 2013. doi: https://doi.org/10.1002/swe.20064. URL `https://agupubs.onlinelibrary.wiley.com/doi/abs/10.1002/swe.20064`.

Paul Tenfjord, Nikolai Østgaard, Kristian Snekvik, Karl Magnus Laundal, Jone Peter Reistad, Stein Haaland, and SE Milan. How the imf by induces a by component in the closed magnetosphere and how it leads to asymmetric currents and convection patterns in the two hemispheres. *Journal of Geophysical Research: Space Physics*, 120(11):9368–9384, 2015.

Frank Toffoletto, Stanislav Sazykin, Robert Spiro, and Richard Wolf. Inner magnetospheric modeling with the rice convection model. *Space science reviews*, 107: 175–196, 2003.

S Tomita, M Nosé, T Iyemori, H Toh, M Takeda, Jürgen Matzka, G Bjornsson, T Saemundsson, A Janzhura, O Troshichev, et al. Magnetic local time dependence of geomagnetic disturbances contributing to the au and al indices. In *Annales Geophysicae*, volume 29, pages 673–678. Copernicus Publications Göttingen, Germany, 2011.

Gábor Tóth, Igor V Sokolov, Tamas I Gombosi, David R Chesney, C Robert Clauer, Darren L De Zeeuw, Kenneth C Hansen, Kevin J Kane, Ward B Manchester,

Robert C Oehmke, et al. Space weather modeling framework: A new tool for the space science community. *Journal of Geophysical Research: Space Physics*, 110 (A12), 2005.

Gabor Toth, Ovsei Volberg, Aaron J Ridley, Tamas I Gombosi, Darren L De Zeeuw, Kenneth C Hansen, David R Chesney, Quentin F Stout, Kenneth G Powell, Kevin J Kane, et al. A physics-based software framework for sun-earth connection modeling. In *Multiscale coupling of Sun-Earth processes*, pages 383–397. Elsevier, 2005.

Bruce T. Tsurutani and Walter D. Gonzalez. The Interplanetary causes of magnetic storms: A review. *Washington DC American Geophysical Union Geophysical Monograph Series*, 98:77–89, January 1997. doi: 10.1029/GM098p0077.

C. L. Waters, B. J. Anderson, and K. Liou. Estimation of global field aligned currents using the iridium® system magnetometer data. *Geophysical Research Letters*, 28 (11):2165–2168, 2001a. doi: https://doi.org/10.1029/2000GL012725. URL `https://agupubs.onlinelibrary.wiley.com/doi/abs/10.1029/2000GL012725`.

CL Waters, BJ Anderson, and K Liou. Estimation of global field aligned currents using the iridium® system magnetometer data. *Geophysical Research Letters*, 28 (11):2165–2168, 2001b.

DR Weimer, NC Maynard, WJ Burke, and C Liebrecht. Polar cap potentials and the auroral electrojet indices. *Planetary and Space Science*, 38(9):1207–1222, 1990. URL `https://doi.org/10.1016/0032-0633(90)90028-0`.

GR Wilson, DR Weimer, JO Wise, and FA Marcos. Response of the thermosphere to joule heating and particle precipitation. *Journal of Geophysical Research: Space Physics*, 111(A10), 2006.

M Wiltberger, RE Lopez, and JG Lyon. Magnetopause erosion: A global view from mhd simulation. *Journal of Geophysical Research: Space Physics*, 108(A6), 2003. URL `https://doi.org/10.1029/2002JA009564`.

M Wiltberger, W Wang, AG Burns, SC Solomon, JG Lyon, and CC Goodrich. Initial results from the coupled magnetosphere ionosphere thermosphere model: Magnetospheric and ionospheric responses. *Journal of Atmospheric and Solar-Terrestrial Physics*, 66(15-16):1411–1423, 2004.

RA Wolf, M Harel, RW Spiro, G-H Voigt, PH Reiff, and C-K Chen. Computer simulation of inner magnetospheric dynamics for the magnetic storm of july 29, 1977. *Journal of Geophysical Research: Space Physics*, 87(A8):5949–5962, 1982.

CC Wu, RJ Walker, and JM Dawson. A three dimensional mhd model of the earth's magnetosphere. *Geophysical Research Letters*, 8(5):523–526, 1981.

N Yokoyama, Y Kamide, and H Miyaoka. The size of the auroral belt during magnetic storms. In *Annales Geophysicae*, volume 16, pages 566–573. Springer, 1998.

Jichun Zhang, Michael W Liemohn, Darren L De Zeeuw, Joseph E Borovsky, Aaron J Ridley, Gabor Toth, Stanislav Sazykin, Michelle F Thomsen, Janet U Kozyra, Tamas I Gombosi, et al. Understanding storm-time ring current development through data-model comparisons of a moderate storm. *Journal of Geophysical Research: Space Physics*, 112(A4), 2007.